ACCSCIENCE PUBLISHING

International Journal of Bioprinting

RESEARCH ARTICLE

Photothermally regulated antimicrobial and osteogenic 3D-printed scaffolds for diabetic cranial bone regeneration

Ye Wang[1,2†], Jiao Hu[2†], Zonghe Xu[1], Qingxia Fang[1,3], Bixia Li[1], Lin Zhou[1,3*], and Dong Wu[1,3*]

[1]School and Hospital of Stomatology, Fujian Medical University, Fuzhou, Fujian, China

[2]Shenzhen Stomatology Hospital (Pingshan) of Southern Medical University, Shenzhen, Guangdong, China

[3]Research Center of Dental and Craniofacial Implants, Fujian Medical University, Fuzhou, Fujian, China

Abstract

Bone regeneration in diabetes-related defects is severely impaired by high-glucose-induced chronic inflammation, oxidative stress, and impaired angiogenesis, resulting in limited repair efficacy of conventional scaffolds in this complex microenvironment. This study constructed a 3D-printed methacrylated dextran (DexMA)/polydopamine-modified hydroxyapatite (P-HAP)/Cu_2O@MXene composite scaffold that integrates photothermal sterilization, osteogenic induction, and immunomodulatory functions. The scaffold utilizes DexMA as a framework to ensure formability and mechanical properties; P-HAP enhances the bioactivity of the inorganic phase; and the Cu_2O@MXene nanocomposite imparts photothermal response and Cu^{2+} release capabilities, enabling programmable temperature control (50 °C for sterilization and 41 °C for osteogenic induction) under near-infrared excitation and local microenvironmental regulation. *In vitro* and *in vivo* experiments demonstrated that the scaffold effectively inhibited inflammatory cytokine expression, promoted M2 macrophage polarization, and synergistically promoted angiogenesis and bone remodeling by increasing CD31 and vascular endothelial growth factor expression and enhancing runt-related transcription factor 2-mediated osteogenic activity. The proposed intelligent scaffold strategy integrates spatiotemporal responsiveness with multiple regenerative mechanisms, offering a promising approach for the repair of complex bone defects under diabetic conditions.

Keywords: Diabetic bone defect; 3D printing scaffold; Osteogenesis; Cu_2O@MXene; Runx2 pathway

1. Introduction

Skull defects are a common and complex form of bone tissue defect in clinical practice.[1] They are often caused by severe trauma, tumor resection, postoperative infection, or congenital developmental abnormalities.[1,2] If not reconstructed in time, they may not only lead to complications such as brain tissue exposure and cerebrospinal fluid leakage, but may also cause abnormal intracranial pressure, neurological dysfunction, and even life-threatening conditions.[2,3] Globally, the demand for skull reconstruction

†*These authors contributed equally to this work.*

***Corresponding authors:**
Lin Zhou
(zhoulin@fjmu.edu.cn);
Dong Wu
(wudong@fjmu.edu.cn)

Citation: Wang Y, Hu J, Xu Z, *et al*. Photothermally regulated antimicrobial and osteogenic 3D-printed scaffolds for diabetic cranial bone regeneration. *Int J Bioprint*. 2026;12(5):026320347. doi: 10.36922/IJB026320347

Received: August 7, 2026

Revised: August 24, 2026

Accepted: August 28, 2026

Published online: August 28, 2026

Copyright: © 2026 Author(s). This is an Open-Access article distributed under the terms of the Creative Commons Attribution License, permitting distribution, and reproduction in any medium, provided the original work is properly cited.

Publisher's Note: AccScience Publishing remains neutral with regard to jurisdictional claims in published maps and institutional affiliations.

surgery has increased steadily, especially in patients with metabolic diseases such as diabetes.[4] Their bone regeneration capacity is severely impaired, manifested as decreased osteogenesis, blocked angiogenesis, and chronic inflammatory activation, which significantly increases the risk of postoperative infection and implant failure.[4,5] Existing clinical data show that the failure rate of bone defect repair in diabetic patients is 1.8 to 3.2 times that of non-diabetic patients, and the wound healing time is prolonged by about 40%, indicating that bone regeneration in the context of diabetes faces more severe challenges.[6] Currently, inert materials such as titanium mesh and polyetheretherketone are commonly used in clinical cranial reconstruction.[7] Although these materials provide excellent mechanical support, they lack bioactivity and tissue integration, are prone to foreign body reactions, infection, and even postoperative bone resorption, making functional regeneration difficult.[8-10] Therefore, there is an urgent need to develop a regenerative material system that combines structural support with biofunctional regulation to address the needs of staged repair of complex bone defects, particularly in the context of metabolic disorders.

In recent years, additively manufactured hydrogel scaffolds have become an important platform in bone tissue engineering because of their favorable biocompatibility, biomimetic microenvironment, and capacity for patient-specific structural design. Beyond geometric customization, recent advances enable the spatial organization of biomaterials, cells, and bioactive cues, as well as the construction of interconnected or perfusable architectures that support vascularization, matrix mineralization, and osteogenic–angiogenic coupling.[11-13] According to ISO/ASTM 52900, additive manufacturing encompasses several process categories with distinct forming mechanisms and material requirements. In material extrusion, scaffolds are constructed through nozzle-based filament deposition and are strongly influenced by ink rheology and filament stability, whereas vat photopolymerization selectively cures liquid photosensitive precursors layer by layer, enabling precise control over scaffold geometry.[14,15] Therefore, clearly defining the specific additive manufacturing process is essential for interpreting scaffold architecture and performance. Hydrogels can simulate the natural extracellular matrix environment through biomimetic design, promote stem cell adhesion and bone differentiation, and can also be loaded with drugs, growth factors, or nanomaterials to enhance their functionality.[16] When combined with additive manufacturing, hydrogel scaffolds precisely match the defect site and provide a bone-regeneration platform that integrates structural control and biological functionality by regulating pore architecture, mechanical properties, and release behavior.[17] Recent studies further demonstrate that the regenerative performance of additively manufactured scaffolds is closely associated with their surface and interfacial characteristics. Chen *et al.*[18] developed a neobavaisoflavone-doped gelatin methacryloyl coating for porous zinc–magnesium scaffolds, which regulated scaffold degradation and ion release while enhancing osteogenic and angiogenic activities. Liu *et al.*[19] further demonstrated that surface roughness, composition, and wettability critically affect the osteogenic performance of three-dimensional (3D)-printed biodegradable zinc-based scaffolds. These findings indicate that the integration of structural design with surface biofunctionalization is essential for effective bone regeneration. However, integrating multifunctional modules providing antibacterial, osteogenic, angiogenic, and immunoregulatory functions, on this basis and achieving "multi-target, multi-stage" precise intervention in diabetic bone defects remains a key bottleneck for current research.

The introduction of functional nanomaterials offers an important means of imparting additional functions to 3D scaffolds. Various metal or metal oxide nanomaterials such as copper(I) oxide (Cu_2O), cerium(IV) oxide (CeO_2), and iron(II,III) oxide (Fe_3O_4) have attracted widespread attention for the treatment of diabetic and infectious bone defects due to their photothermal, ion-regulatory, antioxidant, and immunomodulatory properties.[20-22] For example, Cu-based nanomaterials can regulate macrophage polarization and promote angiogenesis by releasing Cu^{2+} ions, while CeO_2 exhibits a strong inhibitory effect on chronic inflammation.[23,24] In addition, MXene-type two-dimensional materials have been gradually introduced into the fabrication of multifunctional bone repair materials due to their high specific surface area, good conductivity, and photothermal conversion efficiency.[25] However, current research focuses on the enhancement of a single function, such as antibacterial or osteogenic induction, and lacks a system design that integrates multi-mechanism coupling, spatial/temporal program control, and microenvironmental response, making it difficult to achieve synergistic intervention in complex diabetic bone defects.

Based on the key pathological hypothesis that infection interferes with osteogenesis, immune–vascular coupling, and repair in diabetic patients, this study proposed and constructed a methacrylated dextran (DexMA)/polydopamine-modified hydroxyapatite (PDA-HAP; denoted as P-HAP in the composite designation)/Cu_2O@MXene composite scaffold fabricated by digital light processing (DLP)-based vat photopolymerization, aiming to achieve multidimensional regulation of

infection clearance, immune remodeling, and osteogenic–angiogenic coupling during bone defect repair (Figure 1). The material composition was selected to integrate process-specific printability with post-fabrication biological functions. Specifically, the scaffold follows a photocurable matrix–bioactive interface–therapeutic nanocomposite design: DexMA enables light-mediated scaffold fabrication, PDA-HAP provides interfacial reinforcement and osteoconductive cues, and Cu_2O@MXene introduces photothermal and microenvironment-regulatory functions after printing. This system utilizes DexMA as the photocurable scaffold matrix, providing suitable formability and structural stability. PDA-HAP improves interfacial compatibility between the inorganic phase and the DexMA matrix while providing osteogenic cues through the release of Ca^{2+} and PO_4^{3-}. Furthermore, the Cu_2O@MXene nanoplatform enhances photothermal conversion and enables near-infrared (NIR)-mediated staged temperature regulation, with approximately 50 °C applied for early infection control and 41 °C used for subsequent mild photothermal stimulation of regeneration.[26] Copper ion release may further contribute to inflammatory regulation and angiogenesis. Mechanistically, the scaffold reduced pro-inflammatory cytokine expression, promoted angiogenesis-related signaling, and enhanced osteogenic differentiation, thereby reconstructing the regenerative microenvironment of infected diabetic bone defects. Overall, this scaffold integrates structural programmability, infection control, and osteogenic–angiogenic regulation, providing a potential engineering strategy for the repair of diabetic infected bone defects.

2. Materials and methods

2.1. Materials

Dextran (Dex; Mw = 70,000 Da) was purchased from Bai Ling Wei Co., Ltd. (China). 4-Dimethylaminopyridine (DMAP), glycidyl methacrylate (GMA), dimethyl sulfoxide (DMSO), copper(II) chloride ($CuCl_2$), hydrochloric acid, and ammonia solution were obtained from Macklin Biochemical Co., Ltd. (China). Tris(hydroxymethyl) aminomethane (Tris), polyvinylpyrrolidone (PVP), and calcium nitrate tetrahydrate ($Ca(NO_3)_2$) were purchased from Aladdin Industrial Corporation (China). Cell Counting Kit-8 (CCK-8; C0038) was purchased from Beyotime Biotechnology (China). Lipopolysaccharide (LPS; derived from *Escherichia coli* O111:B4; L2630) was purchased from Sigma-Aldrich (United States of America [USA]). Phorbol 12-myristate 13-acetate was purchased from Solarbio Life Sciences (China). Calcein-AM/PI Double Staining Kit (KGAF001) was purchased from Jiangsu Kaijie Biotechnology Co., Ltd. (China). Matrigel was purchased from Corning Inc. (USA). Anti-CD206 antibody (60143-1-Ig) and anti-inducible nitric oxide synthase (iNOS) antibody (18985-1-AP) were purchased from Proteintech Group (China). All cell culture reagents were purchased from Gibco (USA). All chemicals were of analytical grade and used as received without further purification.

2.2. Material preparation and synthesis

2.2.1. Synthesis of methacrylated dextran

Dextran (10.0 g) was dissolved in 100 mL DMSO, after which DMAP (2.0 g) was added as a catalyst, and the mixture was stirred for 1 h. GMA (3.0 mL) was then added, and the reaction mixture was maintained at 25 °C in the dark for 48 h. The product was dialyzed against deionized water for 3 days using a dialysis membrane with a molecular weight cutoff of 3,500 Da (MD3577, Shanghai Yuanye Bio-Technology Co., Ltd., China), lyophilized, and stored at −20 °C.[27]

2.2.2. Synthesis of hydroxyapatite and polydopamine-modified hydroxyapatite

Hydroxyapatite (HAP) was synthesized by adding 0.3 M $(NH_4)_2HPO_4$ solution (Shanghai Macklin Biochemical Co., Ltd., China) to 0.5 M $Ca(NO_3)_2$ solution (Merck KGaA, Germany) under vigorous stirring at a Ca/P molar ratio of 1.67. The pH was adjusted to above 10 using ammonia water, and the reaction was carried out at 37 °C for 24 h. The resulting precipitate was collected by centrifugation, washed with deionized water, and dried at 80 °C. For PDA-HAP, a 10% HAP suspension was prepared and added to Tris buffer containing 8% dopamine hydrochloride (Shanghai Macklin Biochemical Co., Ltd., China), and stirred at room temperature for 24 h. The product was thoroughly washed with deionized water and dried for later use.[28]

2.2.3. Synthesis of Ti_3C_2@MXene

Lithium fluoride (2.0 g; Shanghai Macklin Biochemical Co., Ltd., China) was first dissolved in 40 mL of 9 M hydrochloric acid with stirring for 10 min. Subsequently, 2.0 g of Ti_3AlC_2 (Shanghai Macklin Biochemical Co., Ltd., China) was slowly added, and the mixture was stirred at 40 °C for 24 h. The resulting suspension was centrifuged at 7,155× *g* for 5 min and repeatedly washed with deionized water until the pH exceeded 5. The obtained Ti_3AlC_2@MXene precipitate was redispersed in deionized water, followed by ultrasonication and gentle agitation. After centrifugation at 700× *g* for 2 min, the supernatant was collected and freeze-dried to yield the MXene precursor.[29]

2.2.4. Synthesis of Cu_2O@MXene

Cu_2O/MXene composite nanosheets were fabricated via

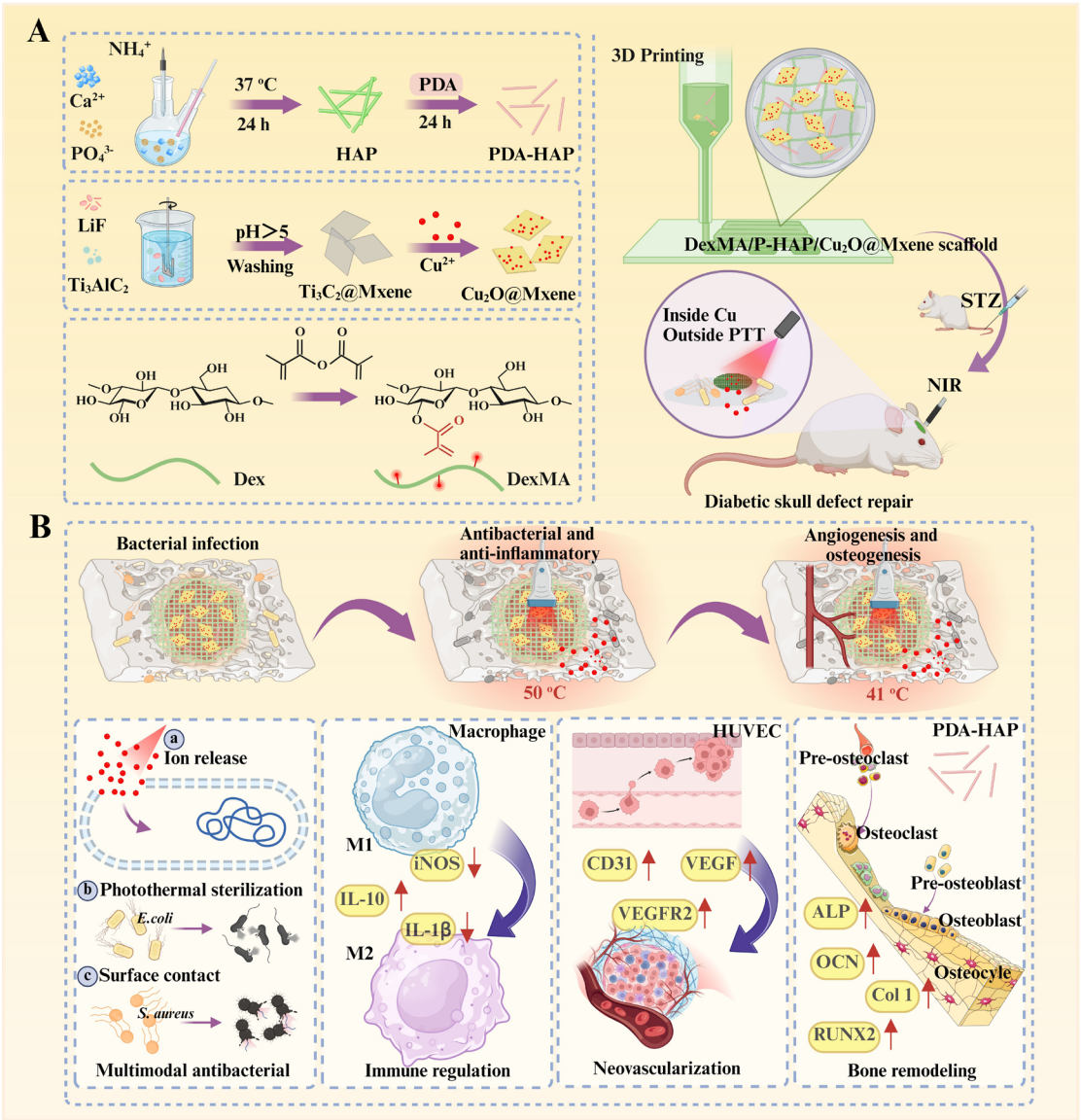


Figure 1. Schematic illustration of the fabrication and therapeutic mechanisms of the 3D-printed DexMA/P-HAP/Cu_2O@MXene composite scaffold for diabetic cranial defect repair. (A) Material preparation and scaffold fabrication: HAP is modified with PDA to form PDA-HAP, thereby enhancing its osteogenic potential and interfacial compatibility. Ti_3C_2 MXene is prepared from Ti_3AlC_2 by LiF-assisted etching and subsequently loaded with Cu_2O to form Cu_2O@MXene, which provides photothermal activity and copper ion release. Dex is methacrylated to form DexMA, which serves as the 3D-printable scaffold matrix. The resulting DexMA/P-HAP/Cu_2O@MXene composite scaffold is fabricated by 3D printing and applied to a STZ-induced diabetic cranial bone defect model under NIR irradiation. (B) Multidimensional repair mechanisms: Under NIR irradiation, the scaffold exerts multiple antibacterial effects, modulates macrophage polarization and inflammatory responses, promotes neovascularization, and enhances osteogenic differentiation and bone modeling, thereby facilitating spatiotemporally coordinated bone repair in the diabetic microenvironment.
Abbreviations: ALP: Alkaline phosphatase; Col1: Collagen type I; Dex: Dextran; DexMA: Methacrylated dextran; HAP: Hydroxyapatite; HUVEC: Human umbilical vein endothelial cell; IL-1β: Interleukin-1 beta; IL-10: Interleukin-10; iNOS: Inducible nitric oxide synthase; LiF: Lithium fluoride; NIR: Near-infrared; OCN: Osteocalcin; PDA: Polydopamine; PDA-HAP: Polydopamine-modified hydroxyapatite; PTT: Photothermal therapy; RUNX2: Runt-related transcription factor 2; STZ: Streptozotocin; VEGF: Vascular endothelial growth factor; VEGFR2: Vascular endothelial growth factor receptor 2.

an *in situ* reduction strategy. Briefly, 50 mg of PVP and 25 mg of $CuCl_2$ were sequentially added to 100 mL of MXene precursor solution (1 mg/mL; Jiangsu Xianfeng Nanomaterials Technology Co., Ltd., China) under magnetic stirring. After stirring for 20 min, 10 mL of freshly prepared $NaBH_4$ solution (0.4 mg/mL; Shanghai Aladdin Biochemical Technology Co., Ltd., China) was introduced dropwise at a rate of 200 μL/min. Following

further stirring for 30 min, the mixture was centrifuged at 4025× *g* for 10 min. The collected precipitate was washed repeatedly with deionized water and anhydrous ethanol and then collected for subsequent use.

2.3. Fabrication of composite scaffolds by digital light processing-based vat photopolymerization

The composite scaffolds were fabricated using DLP-based vat photopolymerization technology (classified according to ISO/ASTM 52900:2021). A printer (EFL-BP-8601P, Engineering For Life, China) equipped with a 405 nm light source was used to perform layer-by-layer selective photopolymerization of the DexMA-based liquid precursor. The designed cylindrical scaffolds featured a diameter of 5.0 mm, a thickness of 1.5 mm, a nominal pore size of 500 μm, a strut width of 300 μm, and a layer thickness of 100 μm, utilizing an alternating 0°/90° structural arrangement. The theoretical porosity, calculated based on the computer-aided design (CAD) model, was approximately 62.5%.

A 25% DexMA solution (containing 0.2% lithium phenyl-2,4,6-trimethylbenzoylphosphinate [Merck KGaA, Germany]) was prepared, and a certain concentration of Cu_2O@Mxene (1mg/mL) and PDA-HAP (1mg/mL) were added to it. The solution was poured into a printer to print the hydrogel (light intensity: 9 mW/cm^2, exposure time: 15 s, number of base layers: 1, base layer exposure time: 18 s). The printed hydrogel scaffolds were rinsed 3–6 times with phosphate-buffered saline (PBS) to obtain the DexMA@P@CM composite scaffolds, where P denotes PDA-HAP and CM denotes Cu_2O@MXene.

To evaluate printing accuracy, the fabricated scaffolds were equilibrated in PBS for 24 h before measurement. Their external diameter and thickness were measured using a digital caliper. Hydrated scaffolds were imaged using a stereomicroscope, and the actual pore size and strut width were quantified using ImageJ (version 1.54t, National Institutes of Health, USA). Five independently fabricated scaffolds were analyzed, with at least 10 pores and 10 struts measured per scaffold.

2.4. Chemical composition and crystal structure characterization

To characterize the structural and chemical properties of the materials, X-ray diffraction (XRD), Fourier transform infrared spectroscopy (FT-IR), proton nuclear magnetic resonance spectroscopy (^{1}H-NMR), and X-ray photoelectron spectroscopy (XPS) were performed. XRD (D8 Advance, Bruker AXS GmbH, Germany) was used to analyze the crystal structure and phase composition. For FT-IR analysis using a Nicolet iS50 spectrometer (Thermo Fisher Scientific, USA), 3–5 mg of each sample was ground with dry KBr (approximately 5% by mass; Merck KGaA, Germany) and pressed into a pellet under vacuum (20 mmHg) for 5 min. Spectra were recorded over the range of 4,000–400 cm^{-1} to characterize changes in the functional groups in the materials. For ^{1}H-NMR analysis using an AVANCE III 400 MHz spectrometer (Bruker BioSpin GmbH, Germany), 8–15 mg of each sample was dissolved in D_2O (Merck KGaA, Germany) and transferred to an NMR tube. The spectra were acquired at room temperature and analyzed using MestReNova software (version 17.0.1, Mestrelab Research S.L.U., Spain). XPS (ESCALAB 250Xi, Thermo Fisher Scientific, United Kingdom) was used to analyze the elemental valence states and binding energies in the composite materials.

2.5. Morphology, particle size distribution, and zeta potential analysis

The micromorphology of the samples was examined using transmission electron microscopy (TEM) and scanning electron microscopy (SEM). For TEM analysis (JEM-2100, JEOL, Japan), the samples were dispersed in anhydrous ethanol at a concentration of 1 mg/mL, sonicated to ensure uniform dispersion, drop-cast onto copper grids, and air-dried before imaging. SEM (GeminiSEM 500, Zeiss, Germany) was used to evaluate the overall morphology, microporous architecture, and surface features of the 3D-printed scaffolds. Elemental composition and spatial distribution were further analyzed by energy-dispersive X-ray spectroscopy (EDS) coupled with SEM. Prior to SEM imaging, the samples were freeze-dried and sputter-coated with gold. In addition, the particle size distribution and zeta potential were determined by dynamic light scattering (Zetasizer Nano ZS90, Malvern, United Kingdom).

2.6. Mechanical and rheological characterization

The mechanical performance of the hydrogels was assessed by compression testing. After demolding, cylindrical hydrogel specimens prepared from 600 μL precursor solution were compressed to failure using a universal testing machine (Instron 3367, Instron, USA). The maximum compressive load was recorded, and the compressive modulus was calculated.

Rheological measurements were carried out using a rheometer (HAAKE MARS 60, Thermo Fisher Scientific, USA) at room temperature. The rheological properties of DexMA hydrogels at concentrations of 15%, 25%, and 35% were evaluated using frequency-sweep and time-sweep measurements. Frequency sweeps were performed over a frequency range of 1–100 Hz at a constant strain of 1%. For the time sweeps, the storage modulus (G′) and loss modulus (G″) were continuously recorded for 300 s at a constant strain of 1% and a frequency of 1 Hz to evaluate the viscoelastic behavior of the hydrogels.

2.7. Analysis of swelling and degradation behavior

In the swelling performance test, the dry hydrogel was weighed (W_0), completely immersed in PBS, and taken out and weighed (W_t) after 1, 2, 4, 6, and 8 h. The swelling ratio was calculated as follows:

$$\text{Swelling ratio (\%)} = (W_t - W_0)/W_0 \times 100\% \quad (1)$$

For the degradation test, scaffold samples (5 mm in diameter and 1.5 mm in height) were freeze-dried to constant weight, and their initial dry weight (W_0) was recorded. Each sample was immersed in 5 mL of phosphate-buffered saline (PBS; pH 7.4) containing either 0 or 10,000 U/mL lysozyme and incubated at 37 °C with continuous shaking at 60 rpm. The degradation medium was completely replaced every 6 h with an equal volume of fresh medium containing the corresponding lysozyme concentration. At predetermined time points of 1, 3, 5, 7, 14, and 21 days, the samples were removed, gently rinsed with deionized water, freeze-dried to constant weight, and weighed to determine the remaining dry weight (W_t). The degradation rate was calculated as follows:

$$\text{Degradation ratio (\%)} = (W_0 - W_t)/W_0 \times 100\% \quad (2)$$

2.8. Evaluation of Cu^{2+} release behavior

A 400 μL hydrogel scaffold was immersed in 3 mL of PBS (pH 7.4) after gelation and incubated at 37 °C under shaking at 1.12× *g*. At predetermined time points (1, 2, 4, 6, 12, 24, 48, 72, and 96 h), the supernatant was collected and replaced with an equal volume of fresh PBS. The collected solutions were centrifuged at 1,789× *g* for 5 min, and the Cu^{2+} concentration was determined using an inductively coupled plasma optical emission spectrometer (Avio 200 ICP-OES, PerkinElmer, USA).[30]

2.9. Evaluation of the photothermal response performance of the scaffold

The photothermal performance of the printed scaffolds was evaluated under 808-nm NIR laser irradiation. The scaffolds were irradiated at 2.0 W/cm^2 for 5 min in a 24-well plate. Infrared thermal images were acquired using an infrared thermal camera (FLIR E6-XT, FLIR Systems, Inc., USA) positioned perpendicular to the sample surface at a fixed distance of 20 cm. Images were acquired before irradiation and at 1-min intervals during the 5-min irradiation period. The emissivity was set to 0.95, and the imaging distance, camera angle, environmental conditions, and temperature display range were kept constant across all experimental groups. Thermal images were analyzed using FLIR Tools software. A circular region of interest (ROI) of uniform size was defined at the center of each sample, and the maximum temperature within the ROI was recorded for quantitative analysis. A thermocouple thermometer (Fluke 52 II, Fluke Corporation, USA) was used only for supplementary spot-temperature measurements and not for infrared image acquisition. Power-dependent heating was evaluated at irradiation intensities of 0.5, 1.0, 1.5, and 2.0 W/cm^2, and four irradiation on/off cycles were performed to assess photothermal stability and reversibility.

2.10. Antibacterial performance evaluation

E. coli and *Staphylococcus aureus* were cultured at 37 °C to the logarithmic phase and adjusted to 1×10^8 CFU/mL. The bacterial suspensions were incubated with different hydrogel scaffold groups for 24 h. Antibacterial activity was first evaluated by plate counting to determine colony-forming units and calculate inhibition rates. Bacterial viability was assessed using SYTO-9/PI fluorescent staining (L7012, Invitrogen™, Thermo Fisher Scientific, USA) and observed under a fluorescence microscope (Eclipse Ti-U, Nikon, Japan), where green and red fluorescence represented live and dead bacteria, respectively. Bacterial morphology and ultrastructural changes after treatment were examined by field-emission SEM (SU8010, Hitachi, Japan). Samples were fixed with 2.5% glutaraldehyde, washed with PBS, deposited onto silicon wafers, air-dried, and sputter-coated with gold prior to imaging. In addition, biofilm formation was evaluated by incubating bacteria with the scaffolds for 48 h, followed by methanol fixation and crystal violet staining (C110702, Shanghai Aladdin Biochemical Technology Co., Ltd., China). The stained biofilms were dissolved, and absorbance at 570 nm was measured using a microplate reader (Multiskan FC, Thermo Fisher Scientific, USA) to quantify biofilm biomass.

2.11. Cellular function and mechanism verification

To comprehensively evaluate the bioactivity and multidimensional functionality of the composite hydrogel scaffold, a systematic *in vitro* characterization system was established. Functional validation was performed in different cell types (bone marrow mesenchymal stem cells [BMSCs; CP-M131], human umbilical vein endothelial cells [HUVECs; CP-H082], and RAW264.7 cells [CL-0190]; obtained from Procell Life Science & Technology Co., Ltd., China). The scaffold's pathway of action was explored in conjunction with relevant molecular mechanisms. The NIR group employed 808 nm laser irradiation (2.0 W/cm^2, 5 min) to activate the photothermal reaction.

2.11.1. Biocompatibility assessment and cell morphology analysis

The biocompatibility of the materials with BMSCs and

HUVECs was assessed using a CCK-8 assay. Briefly, cells were seeded in 96-well plates and incubated with material extracts (material-to-medium ratio = 1 g:10 mL, 24 h extraction). Cell viability was measured on days 1, 3, and 5 by recording absorbance at 450 nm. Live/dead staining was further performed using a Calcein-AM/PI dual staining kit. Cells were cultured in 48-well plates, incubated with extracts for 24 h, stained in the dark for 30 min, and imaged using an inverted fluorescence microscope. For cytoskeletal analysis, F-actin and nuclei were labeled with FITC-phalloidin (Beyotime Biotechnology, China) and DAPI (Beyotime Biotechnology, China), respectively. Cell adhesion, spreading, and morphology were evaluated at designated time points using fluorescence microscopy.

2.11.2. Cell migration assay

The effect of the materials on HUVEC migration was evaluated using scratch wound and Transwell assays. For the wound healing assay, a linear scratch was created on a confluent HUVEC monolayer using a sterile pipette tip. After washing with PBS, undiluted material extract (100%), prepared at a material-to-medium mass-to-volume ratio of 1 g:10 mL (0.1 g/mL), was added. Images were captured at 0, 12, 24, and 36 h, and the wound closure area was quantified using ImageJ. For the Transwell assay, HUVECs (1×10^5 cells/well) suspended in serum-free medium were seeded into the upper chamber of Transwell inserts (8.0 μm pore size; Corning, USA). The lower chamber was filled with medium containing different extracts and 10% fetal bovine serum. After 24 h of incubation, the migrated cells were fixed, stained, and counted under a microscope to assess migration ability.

2.11.3. Assessment of angiogenic potential

Suspensions of HUVECs (1×10^4 cells/well) were seeded in Matrigel-coated 96-well plates and incubated with the material extract for 6 h. The total length, number of nodes, and number of branches of the formed capillary-like structures were photographed and counted under a microscope. To further explore the molecular mechanisms, immunofluorescence staining was performed to detect the expression of CD31, vascular endothelial growth factor (VEGF), and vascular endothelial growth factor receptor 2 (VEGFR2), and mean fluorescence intensity was analyzed using ImageJ. Furthermore, after protein extraction, Western blotting was performed to detect VEGF and CD31, key factors associated with angiogenesis, to clarify the angiogenic mechanism.[31]

2.11.4. Analysis of osteogenic induction ability

Bone marrow mesenchymal stem cells were seeded in 24-well plates at a density of 2×10^4 cells/mL and subsequently cultured in fresh hydrogel extract. Alkaline phosphatase (ALP) staining was performed on day 7 using an ALP staining kit (C3206; Beyotime Biotechnology, China), and ALP activity was quantified by measuring the absorbance at 405 nm using a multifunction microplate reader. Alizarin Red S staining (C0148S; Beyotime Biotechnology, China) was performed on day 14 to assess the formation of mineralized nodules. The stained mineralized nodules were subsequently quantified by measuring the absorbance at 562 nm after dye extraction with anhydrous ethanol.

Immunofluorescence staining was performed to assess the expression of the osteogenic markers runt-related transcription factor 2 (RUNX2), type I collagen (COL-I), and osteocalcin (OCN). Cells were incubated overnight at 4 °C with rabbit anti-RUNX2 (1:200; ab236639), rabbit anti-COL-I (1:200; ab34710), or rabbit anti-OCN (1:200; ab93876) primary antibodies (Abcam, United Kingdom [UK]). After washing, the cells were incubated with Alexa Fluor 488-conjugated goat anti-rabbit IgG (H+L) secondary antibody (1:500; ab150077, Abcam, UK) for 1 h at room temperature in the dark. Nuclei were counterstained with DAPI (1 μg/mL; C1002, Beyotime Biotechnology, China).

Western blotting was performed to assess the protein expression levels of RUNX2, ALP, OCN, and β-catenin. Membranes were incubated overnight at 4 °C with primary antibodies against RUNX2 (1:1,000; 20700-1-AP), ALP/ALPL (1:1,000; 11187-1-AP), OCN (1:1,000; 23418-1-AP), β-catenin (1:1,000; 51067-2-AP), or GAPDH (1:5,000; 60004-1-Ig). After washing, the membranes were incubated with the appropriate HRP-conjugated goat anti-rabbit IgG (H + L) (1:5,000; SA00001-2) or HRP-conjugated goat anti-mouse IgG (H + L) (1:5,000; SA00001-1) secondary antibody. All antibodies used for Western blotting were obtained from Proteintech Group (China).

2.11.5. Verification of macrophage polarization and immune modulation

Using RAW264.7 cells as a model, the material's regulatory effects on macrophage immune phenotype were investigated. Under inflammatory conditions induced by LPS (5 μg/mL), the cells were exposed to the extracts from each group. After 24 hours of culture, Real-time quantitative polymerase chain reaction (RT-qPCR) was performed to assess the expression levels of M1 phenotype factors (interleukin-1 beta [IL-1β]) and M2 phenotype factors (interleukin-10 [IL-10]). Immunofluorescence staining was performed to detect CD86 and CD206 protein expression at excitation wavelengths of 555 nm and 488 nm, respectively, to visualize M1/M2 polarization trends. Flow cytometry (FACSAria III, BD Biosciences, USA) was

used to quantify the ratio of $CD86^+$ (M1) to $CD206^+$ (M2) cells, assessing the distribution of immune polarization induced by the material and reflecting its potential to modulate the inflammatory microenvironment.

2.11.6. Real-time quantitative polymerase chain reaction

RAW264.7 cells (5×10^5 cells/well) were seeded in 12-well plates and stimulated with LPS (5 μg/mL) overnight, followed by treatment with hydrogel extracts for 24 h. Total RNA was extracted using TRIzol and quantified with a NanoDrop 2000 (Thermo Fisher Scientific, USA). Complementary DNA was synthesized by reverse transcription, followed by RT-qPCR using an ABI 7500 Real-Time PCR System and SYBR Premix Ex Taq (Takara, Japan). *Gapdh* was used as an internal control, and the relative expression levels of *Il1b* and *Il10* were calculated using the $2^{-\Delta\Delta Ct}$ method.

2.11.7. Western blotting

Human umbilical vein endothelial cells and BMSCs were seeded in 6-well plates and, after attachment, treated with the hydrogel extracts from each group for 24 h. The cells were lysed with RIPA buffer, and the lysates were centrifuged. Protein concentrations were quantified before equal amounts of protein were separated by sodium dodecyl sulfate–polyacrylamide gel electrophoresis and transferred onto polyvinylidene fluoride membranes. After blocking, the membranes were incubated with the corresponding primary antibodies, followed by horseradish peroxidase (HRP)-conjugated secondary antibodies. Protein bands were detected using an enhanced chemiluminescence substrate and imaged using a ChemiDoc MP Imaging System (Bio-Rad, USA). Band intensities were quantified using ImageJ.

2.11.8. Molecular mechanism and pathway verification

Total RNA was extracted from BMSCs using TRIzol, quantified using a NanoDrop spectrophotometer, and assessed for RNA integrity using an Agilent 2100 Bioanalyzer (Agilent Technologies, Inc., USA), with an RNA integrity number ≥ 7.0 required for subsequent analysis. Strand-specific libraries were constructed and subjected to 150-bp paired-end sequencing on a NovaSeq 6000 platform (Illumina, USA), generating ≥ 6 GB of sequencing data per sample. Raw reads were processed using fastp and aligned to the mouse reference genome GRCm38/mm10 using HISAT2. Differentially expressed genes were identified using DESeq2 with thresholds of $|\log_2 \text{fold change}| \geq 1$ and $p < 0.05$. Gene Ontology (GO) and Kyoto Encyclopedia of Genes and Genomes (KEGG) enrichment analyses were performed using clusterProfiler.

2.12. Establishment of an infected calvarial defect model in diabetic rats and evaluation of treatment effects

2.12.1. Animal grouping

Thirty-six male Sprague–Dawley rats (200–220 g) were randomly assigned to six groups (n = 6 rats per group): Control, DexMA, DexMA@P, DexMA@P+NIR, DexMA@P@CM, and DexMA@P@CM+NIR. Two bilateral calvarial defects were created in each rat, and both defects in the same animal received the same treatment. The day-3 antibacterial assessment was performed non-terminally in all animals (n = 6 rats per group). Subsequently, three rats from each group were euthanized at 6 weeks, and the remaining three rats from each group were euthanized at 12 weeks (n = 3 rats per group at each terminal time point). Measurements obtained from the two defects in each animal were averaged and treated as a single biological replicate. All animals were housed under specific pathogen-free conditions with free access to food and water. The study was conducted in accordance with the Principles of Laboratory Animal Care (National Institutes of Health Publication No. 85-23, revised 1996) and was approved by the National Institutional Animal Care Committee (approval no. 202501007).

2.12.2. Establishment of an infected calvarial defect model in diabetic rats

An infected calvarial defect model was established in diabetic rats to evaluate scaffold efficacy. Diabetes was induced by intraperitoneal injection of STZ (50 mg/kg in 0.1 M citrate buffer, pH 4.5) for three consecutive days. Rats with fasting blood glucose levels > 16.7 mmol/L for two consecutive days were considered diabetic. A mixed bacterial suspension of *S. aureus* and *E. coli* (1:1; 1×10^8 CFU/mL) was used to inoculate the scaffolds by immersion for 2 h. Bilateral 5-mm-diameter critical-size calvarial defects were created, and the inoculated scaffolds were implanted into the defects. Postoperative photothermal treatment was performed using an 808-nm laser, with the treatment-site temperature maintained at 50 ± 1 °C for 5 min/day on postoperative days 1–3 and at 41 ± 1 °C three times per week thereafter. Animals were euthanized at 6 and 12 weeks for subsequent evaluation.[32,33]

2.12.3. In vivo antibacterial performance evaluation

On postoperative day 3, all six rats in each group (n = 6 rats per group) were anesthetized for non-terminal antibacterial assessment. Under aseptic conditions, the surgical area was exposed, and exudate from the implanted scaffolds and surrounding tissues was collected using

sterile swabs without removing the scaffolds or harvesting tissue. Each swab was immediately transferred to 1 mL of sterile PBS and vortexed for 1 min to release adherent bacteria. The resulting bacterial suspensions were serially diluted with sterile PBS and plated on Luria–Bertani (LB) agar. After incubation at 37 °C for 24 h, colonies were counted, and the bacterial burden was expressed as colony-forming units (CFU) per sampling site. After sampling, the surgical area was disinfected and reclosed. Following this non-terminal assessment, three rats from each group were euthanized at 6 weeks, and the remaining three rats from each group were euthanized at 12 weeks.

2.12.4. Photothermal image evaluation

To verify the *in vivo* photothermal conversion capacity and spatial localization of the photothermal effect of the 3D-printed scaffolds under NIR laser irradiation, infrared thermal images of the surgical site were acquired immediately after surgery and at different time points. An 808-nm NIR laser (power density: 2 W/cm^2) was applied to the surgical area for 5 min. Simultaneously, an infrared thermal imager (FLIR E60, FLIR Systems, USA) was used to record surface temperature changes and their spatial distribution in the different groups in real time.

2.12.5. Micro-computed tomography imaging and bone quantification analysis

Calvarial specimens were collected at 6 and 12 weeks postoperatively and imaged using a micro-computed tomography (CT) system (SkyScan 1176, Bruker microCT, Belgium). The scanning parameters were 65 kV and 380 μA, with a voxel size of 18 μm. 3D reconstruction of the defect area was performed using NRecon and CTAn software (version 1.7.4.2; Bruker microCT, Belgium). Parameters including bone volume fraction (BV/TV), trabecular number (Tb.N), trabecular thickness (Tb.Th), and trabecular spacing were analyzed to assess the amount and microstructure of newly formed bone.

2.12.6. Histological staining

Fixed skull tissue was decalcified, paraffin-embedded, and sectioned at a thickness of 5 μm. Hematoxylin and eosin and Masson's trichrome staining were performed to assess tissue structure and collagen deposition, respectively. Additionally, Goldner's trichrome staining was performed to evaluate mineralized bone formation and bone remodeling.

2.12.7. Immunofluorescence detection of osteogenic and angiogenic marker expression

Immunofluorescence staining was used to detect proteins associated with new bone formation and angiogenesis, including osterix (OSX), COL-I, and CD31. Sections were deparaffinized, subjected to antigen retrieval, and blocked with bovine serum albumin. The sections were then incubated with primary antibodies overnight at 4 °C, followed by fluorescently labeled secondary antibodies for 1 h at room temperature. Cell nuclei were counterstained with DAPI. Images were acquired using a confocal microscope (A1R, Nikon Corporation, Japan), and the fluorescence intensity and area of positively stained regions were quantified using ImageJ.

2.12.8. Immunohistochemical analysis of inflammatory cytokine expression

To evaluate regulation of the local inflammatory microenvironment, immunohistochemical staining for tumor necrosis factor alpha (TNF-α), IL-1β, and interleukin 6 (IL-6) was performed. After deparaffinization and antigen retrieval, the sections were incubated with primary antibodies overnight, followed by HRP-conjugated secondary antibodies. The signals were visualized using 3,3′-diaminobenzidine, and the sections were counterstained with hematoxylin. Images were captured under a light microscope, and the positively stained area was quantified using ImageJ.

2.13. Statistical analysis

All data are presented as mean ± standard deviation. Statistical analyses were performed using GraphPad Prism 9.0 (GraphPad, USA). Differences between two groups were analyzed using an unpaired Student's *t*-test, and multiple-group comparisons were performed using one-way ANOVA followed by Tukey's post hoc test. A p-value < 0.05 was considered statistically significant. All experiments were repeated at least three times. Significance levels were defined as $^*p < 0.05$, $^{**}p < 0.01$, $^{***}p < 0.001$.

3. Results and discussion

3.1. Structure confirmation and dispersion stability evaluation of composite nanomaterials.

In this study, we successfully synthesized and systematically characterized the key nanocomponents of the DexMA/P-HAP/Cu_2O@MXene composite scaffold. TEM images (Figure 2A) revealed that HAP exhibits regular nanorod morphology with uniform particle size and smooth surfaces.[34] Following PDA modification, a uniform coating layer appeared on the particle surfaces, confirming successful PDA attachment to HAP surfaces. This modification enhanced particle surface activity and subsequent functionalization potential. XRD results (Figure 2B) revealed that the diffraction peaks of the synthesized HAP closely match those of the standard card

(JCPDS 73-0293), exhibiting characteristic peaks at (100), (002), (211), and (300), indicating the phase purity of the sample.[35] The major diffraction peaks remained unchanged after PDA modification, suggesting no alteration to the HAP crystal structure. The FT-IR spectrum (Figure 2C) further confirmed the modification effect. HAP exhibited characteristic absorption bands at 564, 603, 962, 1,032, and 1,094 cm^{-1}, corresponding to the bending and stretching vibrations of phosphate groups. The absorption peak at 871 cm^{-1} corresponded to HPO_4^{2-}, while those at 3,570 cm^{-1} and 633 cm^{-1} represented hydroxyl stretching vibrations. The band at approximately 1,641 cm^{-1} likely arose from hydroxyl groups corresponding to water absorbed from the atmosphere during the experiment.[34] Following PDA modification, the O–H stretching vibration peak around 3,400 cm^{-1} indicated abundant surface hydroxyl groups. This peak broadened and intensified due to the overlapping stretching vibrations of both –OH and –NH groups present in dopamine, confirming successful PDA encapsulation on the HAP surface. In PDA-HAP, in addition to retaining the typical phosphate and hydroxyl absorption peaks of HAP, characteristic peaks such as C–N and aromatic C = C appeared. The enhanced and broadened O–H stretching peak indicated the successful introduction of the dopamine coating layer.

Scanning electron microscopy images and EDS elemental mapping (Figure 2D) revealed uniform loading of Cu_2O nanoparticles on the MXene sheet surfaces. The EDS spectrum (Figure 2E) confirmed the presence of Cu, Ti, and O, supporting the presence and spatial colocalization of Cu, Ti, and O. XRD patterns (Figure 2F) showed characteristic MAX-phase peaks in Ti_3AlC_2, with increased interlayer spacing in MXene after Al layer removal.[36] Following Cu_2O loading, diffraction peaks at 2θ = 36.4°, 42.3°, and 61.3° appeared, corresponding to the (111), (200), and (220) crystal planes of Cu_2O, further confirming its successful incorporation. XPS analysis (Figure 2G) similarly detected Ti 2p and C 1s signals from MXene. In Cu_2O@MXene, a new Cu 2p peak (approximately 932.5 eV) appeared, while the O 1s peak morphology changed, indicating that the presence of Cu_2O altered the surface chemical state of the material. Meanwhile, the Tyndall effect demonstrated the dispersion of the materials. Results showed (Figure 2H) that no significant light scattering was observed in pure water, while the PDA-HAP aqueous solution exhibited faint scattered light paths. In contrast, the Cu_2O@MXene dispersion displayed distinct light paths, indicating the formation of a stable colloid in the aqueous solution. Zeta potential measurements (Figure 2I) showed values of −37.1 mV for MXene and −16.8 mV for Cu_2O@MXene, both within stable ranges, confirming excellent dispersion. The decrease in absolute potential indicated that the introduction of Cu_2O altered the overall surface charge distribution. This change enhanced colloidal stability and may modulate interactions with cells. The particle size distribution results (Figure 2J) further verified the effect of structural modification on particle size. The average particle size of HAP was 218.3 ± 7.91 nm, with a narrow distribution. The average particle size of PDA-HAP was 236.3 ± 19.11 nm, slightly larger than that of HAP, consistent with the addition of the PDA coating layer. The average particle size of MXene was 256.8 ± 4.66 nm, with a relatively wide distribution, reflecting its heterogeneous lamellar structure. The average particle size of Cu_2O@MXene further increased to 399.4 ± 31.18 nm, indicating that the loading of Cu_2O significantly increased the overall particle size. Therefore, these materials not only maintained good crystal structure and dispersibility but also exhibited controllable surface modification and suitable particle size characteristics, laying a solid material foundation for their application in 3D-printed photothermal composite scaffolds.

3.2. Structural controllability and functional performance evaluation of 3D-printed scaffolds.

To verify the comprehensive performance of the constructed DexMA@P@CM 3D-printable scaffold in terms of mechanical strength, structural stability, and intelligent responsiveness, this study conducted a systematic physicochemical and functional evaluation. First, ^{1}H-NMR and FT-IR confirmed the successful grafting of Dex with methacrylic acid groups. The ^{1}H NMR spectrum (Figure 3A) reveals characteristic double-bond hydrogen peaks at 5.67 ppm and 6.12 ppm in DexMA, distinct from the Dex signal, indicating successful double-bond introduction.[37,38] The FT-IR spectrum (Figure 3B) further reveals the presence of a stretching vibration peak at 1,702 cm^{-1}, corresponding to the C = C double bond of the methacrylic acid group, and a reduction in the hydroxyl absorption peak at 3,440 cm^{-1}.[27] This further validates the effectiveness of the methacrylation reaction for enabling photocrosslinking and provides a foundation for subsequent 3D printing and mechanical property manipulation. The scaffold was designed with a nominal pore size of 500 μm, a theoretical porosity of approximately 62.5%, and a 0°/90° alternating architecture to generate interconnected channels. Representative macroscopic top and side images (Figure A1) showed that both DexMA and DexMA@P@CM scaffolds maintained the intended cylindrical geometry. The cross-sectional images further demonstrated the preservation of the layered, interconnected internal architecture after the incorporation of PDA-HAP and Cu_2O@MXene. SEM images (Figure 3C) showed that DexMA formed a regular grid-like structure

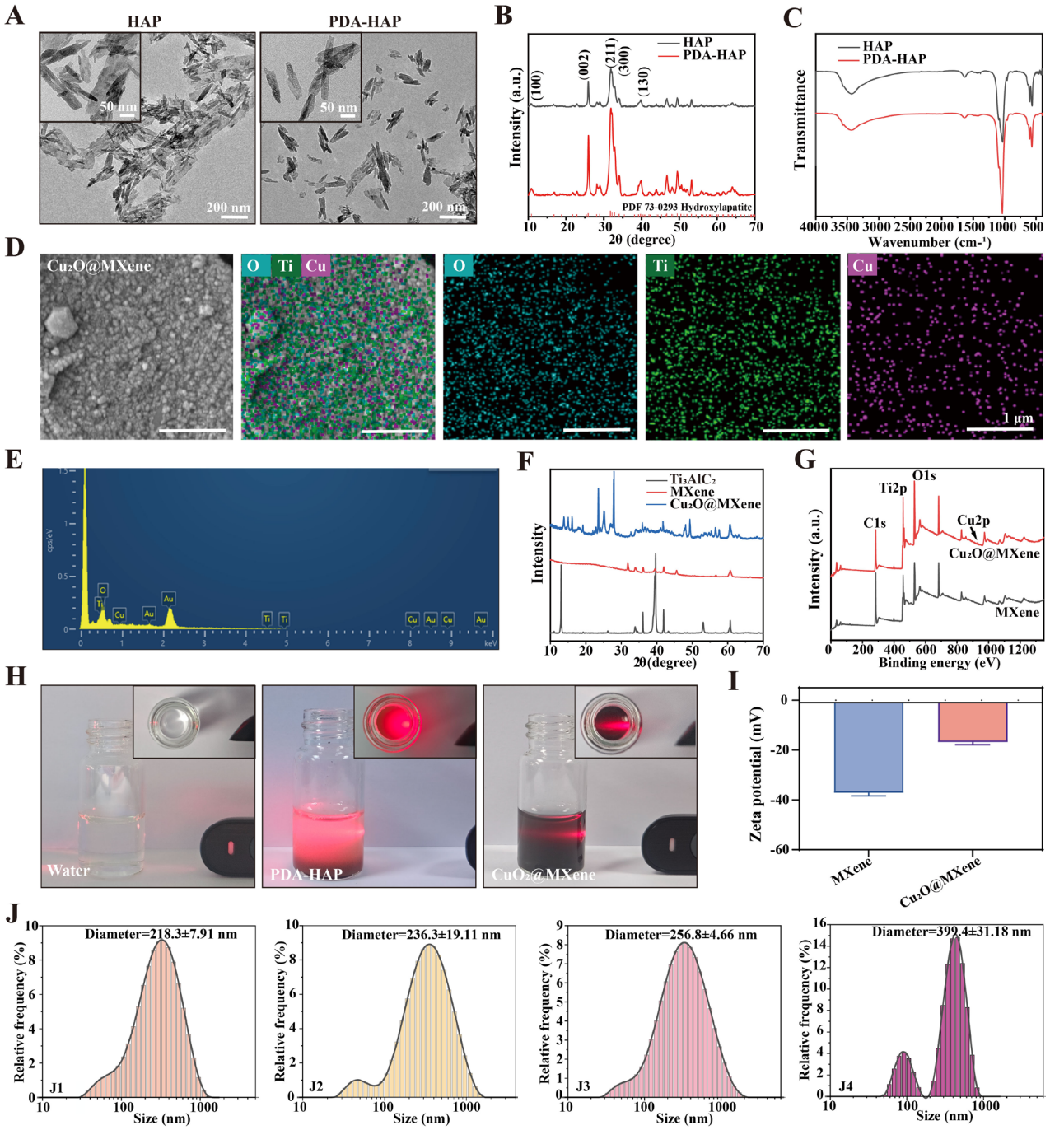


Figure 2. Chemical structure characterization of nanoparticles. (A) Transmission electron microscopy images of HAP and PDA-HAP. Scale bars: 200 nm; magnification: 50,000×. Insets: Scale bars: 50 nm; magnification: 200,000×. (B) XRD patterns of HAP and PDA-HAP. (C) Fourier transform infrared spectra of HAP and PDA-HAP. (D) Scanning electron microscopy image and EDS mapping of Cu_2O@MXene. Scale bars: 1 μm; magnification: 20,000×. (E) EDS spectrum of Cu_2O@MXene. (F) XRD patterns of Ti_3AlC_2, MXene, and Cu_2O@MXene. (G) X-ray photoelectron spectra of MXene and Cu_2O@MXene. (H) Tyndall effect of water, PDA-HAP aqueous solution, and Cu_2O@MXene aqueous solution. (I) Zeta potential of MXene and Cu_2O@MXene. (J) Particle size distribution histograms of nanoparticles (J1–J4 represent HAP, PDA-HAP, MXene, and Cu_2O@MXene, respectively).

Abbreviations: EDS: Energy-dispersive X-ray spectroscopy; HAP: Hydroxyapatite; PDA-HAP: Polydopamine-modified hydroxyapatite; XRD: X-ray diffraction.

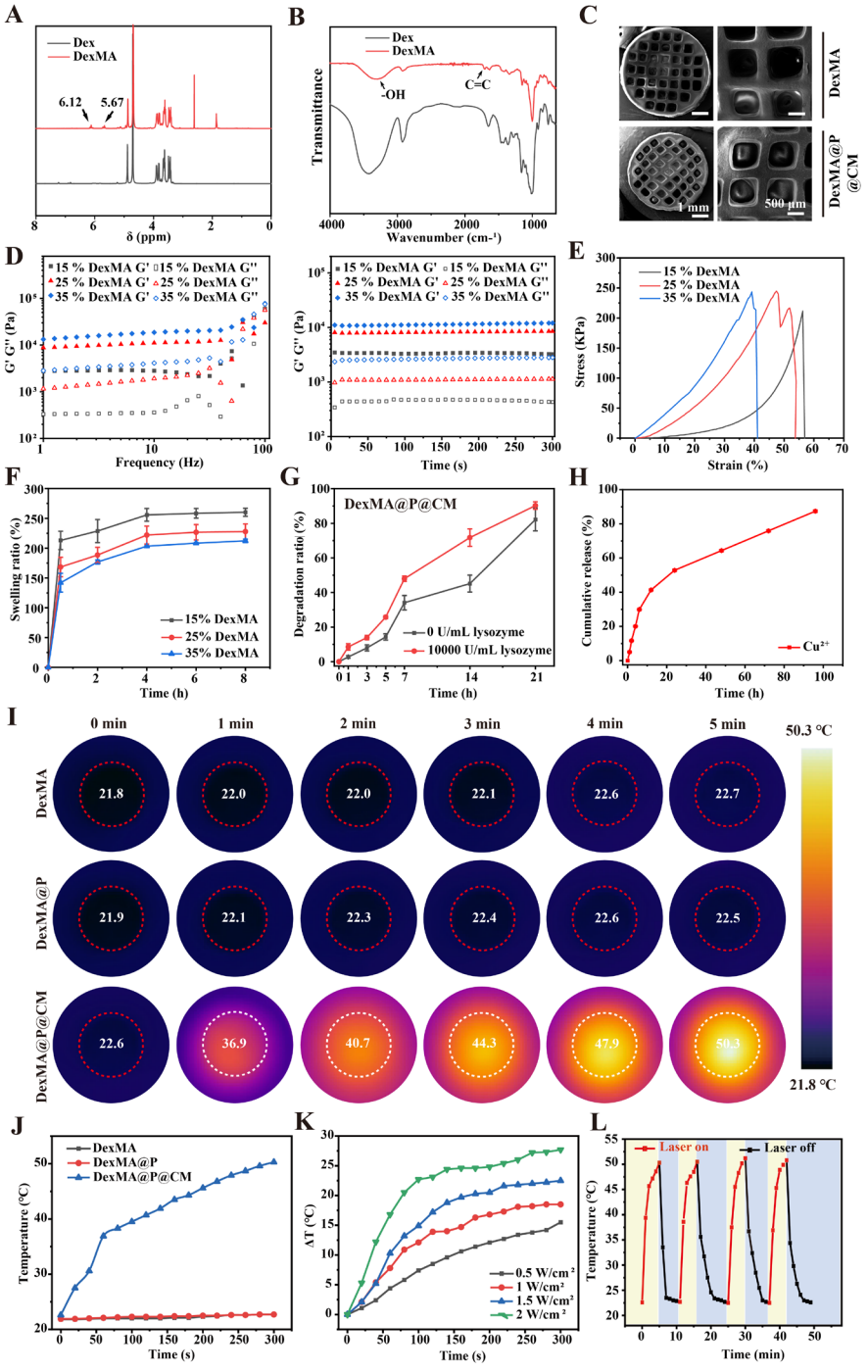


Figure 3. Preparation and performance characterization of 3D-printed scaffolds. (A) Proton nuclear magnetic resonance spectra of Dex and DexMA. (B) Fourier transform infrared spectra of Dex and DexMA. (C) Scanning electron microscopy images of DexMA and DexMA@P@CM scaffolds. Scale bars: left: 1 mm, magnification: 40×; right: 500 μm, magnification: 150×. (D) Rheological frequency and time-scan curves of 15%, 25%, and 35% DexMA hydrogels. (E) Compressive stress-strain curves of 15%, 25%, and 35% DexMA hydrogels. (F) Swelling performance curves of 15%, 25%, and 35% DexMA hydrogels. (G) Degradation rate curves of DexMA@P@CM scaffolds under different external environments. (H) Cumulative release curve of Cu^{2+} from DexMA@P@CM scaffolds at designated time points. (I) Infrared thermography of DexMA, DexMA@P, and DexMA@P@CM scaffolds in deionized water. NIR conditions: 808 nm, 2.0 W/cm^2, height: 15 cm. (J) Photothermal heating curve of 3D-printed scaffolds immersed in deionized water under NIR irradiation. (K) Photothermal heating curve of DexMA@P@CM scaffolds at different NIR powers. (L) Cyclic heating curve of DexMA@P@CM scaffolds undergoing four on/off cycles in deionized water.
Abbreviations: Dex: Dextran; DexMA: Methacrylated dextran; NIR: Near-infrared.

with uniformly arranged pores. Following the incorporation of PDA-HAP and Cu_2O@MXene, the DexMA@P@CM scaffold retained its overall structural integrity, indicating that the functional components did not substantially disrupt scaffold formation. Quantitative dimensional analysis showed that the hydrated scaffolds had an external diameter of 5.08 ± 0.06 mm, a thickness of 1.56 ± 0.04 mm, a pore size of 462 ± 28 μm, and a strut width of 326 ± 21 μm, compared with the corresponding CAD values of 5.00 mm, 1.50 mm, 500 μm, and 300 μm, respectively. The corresponding absolute dimensional deviations were 1.6%, 4.0%, 7.6%, and 8.7%. The slight reduction in pore size and increase in strut width were likely caused by light scattering and lateral overcuring during vat photopolymerization, whereas the minor deviations in overall dimensions may also be associated with post-printing swelling. Overall, the fabricated scaffolds reproduced the intended architecture with acceptable, although not perfect, dimensional fidelity. This interconnected macroporous architecture is expected to facilitate mass transport, vascular infiltration, and tissue ingrowth.[39]

In terms of mechanical control, rheological and compression testing (Figure 3D and 3E) further revealed the balance between material concentration and structural density. DexMA at 35% exhibited the highest modulus and stress-bearing capacity, but this high concentration resulted in decreased flexibility. In contrast, DexMA at 15% exhibited poor morphology due to excessive swelling (Figure 3F). Based on the tested formulations, DexMA at 25% was selected because it provided the most appropriate balance among formability, mechanical strength, and swelling stability. Furthermore, the DexMA@P@CM scaffold exhibited dual properties: biodegradability and therapeutic activity. Degradation experiments (Figure 3G) demonstrated accelerated degradation in the presence of lysozyme, meeting the basic requirements of a biodegradable implant. To impart therapeutic properties, Cu_2O@MXene was incorporated into the scaffold, providing antibacterial properties and photothermal responsiveness. The sustained-release curve of Cu^{2+} (Figure 3H) showed that the material stably released nearly 90% of Cu^{2+} over 96 h, demonstrating excellent ion-release stability and potential advantages in infection control and vascularization promotion.[40] Regarding photothermal performance, thermal imaging (Figure 3I) revealed that the temperature of DexMA@P@CM rapidly increased under NIR laser irradiation (808 nm, 2.0 W/cm^2), reaching 50.3 °C within 5 min and significantly exceeding the temperatures observed for the DexMA and DexMA@P groups. This finding indicated that the introduction of the functional Cu_2O@MXene composite significantly enhanced photothermal conversion.[41] Further temperature rise curves (Figure 3J) also showed that the temperature of DexMA@P@CM rose rapidly over a short period and then stabilized, making it suitable for mild photothermal therapy. The power gradient test (Figure 3K) confirmed that the temperature rise amplitude was proportional to the laser power and was controllable; the cyclic switching experiment (Figure 3L) showed that DexMA@P@CM exhibited excellent photothermal response reversibility and cyclic stability, and maintained good performance in multiple heating/cooling cycles, ensuring the continuity and safety of the thermal effect in practical applications. These results also clarify the rationale for the scaffold composition. DexMA primarily ensures photocurable fabrication and structural stability, whereas PDA-HAP and Cu_2O@MXene mainly provide osteogenic and photothermal functions after printing. Consistent with previous studies showing that biomaterial composition influences both printing performance and the mechanical and thermal properties of fabricated scaffolds,[42,43] the present formulation maintained a regular printed architecture while integrating multiple therapeutic functions. However, direct benchmarking against other scaffold systems was not performed because of differences in materials, fabrication processes, and testing conditions. In summary, the DexMA@P@CM scaffold not only exhibits good structural printability and mechanical strength, but also controllable degradation, adjustable photothermal properties, and functional ion-release characteristics, suggesting broad potential for application in the repair of diabetic skull defects.

3.3. Evaluation of photothermal synergistic antibacterial properties of 3D-printed scaffolds.

To systematically evaluate the antibacterial properties of the constructed 3D-printed scaffolds, co-culture antibacterial experiments, biofilm inhibition assays, Live/Dead staining, and SEM were conducted to assess the effects against two typical pathogens, *E. coli* and *S. aureus* (Figure 4). In Figure 4A, after co-culture of each scaffold with *E. coli* and *S. aureus* for 24 h, the bacterial broth was plated on LB agar plates and observed for colony growth. The results showed that the DexMA, DexMA@P, and DexMA@P+NIR groups exhibited dense colony growth, similar to that of the control group, indicating no significant antibacterial activity. In contrast, the DexMA@P@CM group showed significantly fewer colonies, whereas the DexMA@P@CM+NIR group showed almost no colony formation, demonstrating the scaffold's potent antibacterial properties under light irradiation. Quantitative analysis results (Figure 4B and 4C) showed that the DexMA@P@CM group exhibited approximately 90.56% and 90.12% inhibition rates against *E. coli* and *S. aureus*, respectively, while the DexMA@P@CM+NIR group exhibited inhibition rates exceeding

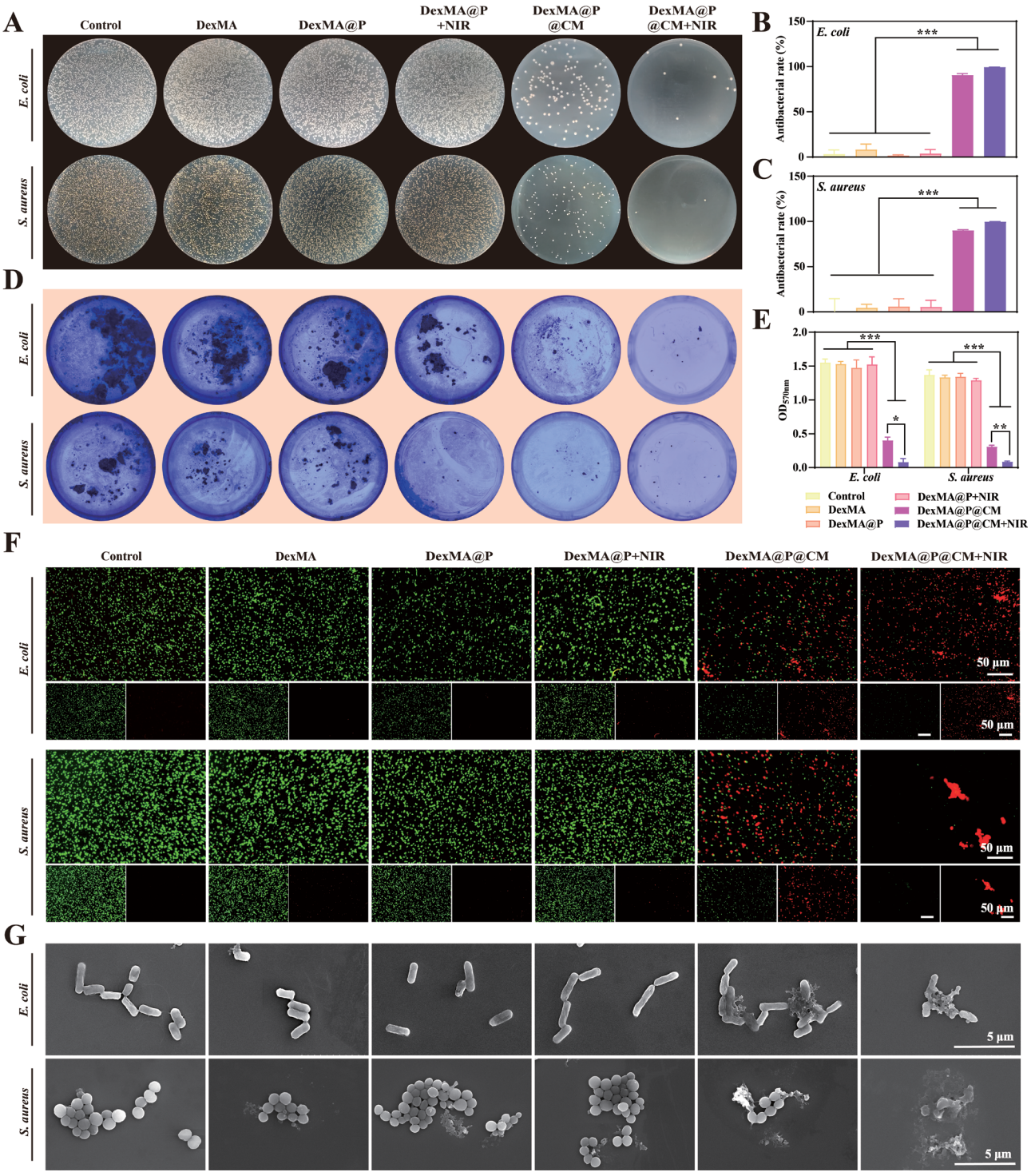


Figure 4. Evaluation of the antimicrobial properties of 3D-printed scaffolds. (A) Agar plate images after co-culturing scaffolds with *E. coli* and *S. aureus*. (B) Quantitative analysis of *E. coli* inhibition rate. (C) Quantitative analysis of *S. aureus* inhibition rate. (D) Crystal violet staining images of biofilms. (E) Absorbance measurements (OD_{570}) after biofilm dissolution. (F) Fluorescent staining images of live/dead bacteria after co-culturing scaffolds with *E. coli* and *S. aureus*. Scale bars: 50 μm; magnification: 200×. (G) Scanning electron microscopy images of bacteria after co-culturing scaffolds with *E. coli* and *S. aureus*. Scale bars: 5 μm; magnification: 5,000×. *$p < 0.05$, **$p < 0.01$, ***$p < 0.001$.
Abbreviations: DexMA: Methacrylated dextran; NIR: Near-infrared.

99%, both with statistically significant differences (***$p < 0.001$), confirming the highly effective antibacterial activity achieved through the synergistic photothermal mechanism. Figure 4D shows the effects of different scaffold groups on biofilm formation by the two bacterial species. Crystal violet staining revealed that a significant amount of biofilm remained in the pores of the DexMA and DexMA@P groups, while the DexMA@P@CM+NIR group exhibited the weakest staining, with virtually no biofilm remaining. Absorbance measurements (Figure 4E) further demonstrated that the DexMA@P@CM+NIR group exhibited significantly lower OD_{570} absorbance than the other groups, demonstrating its effective inhibitory effect on bacterial biofilm formation. Live/Dead fluorescence staining was used to further analyze bacterial activity (Figure 4F), with green representing live bacteria and red representing dead bacteria. The results showed that abundant green signals were observed in the DexMA and DexMA@P groups, whereas the DexMA@P@CM+NIR group showed predominantly red fluorescence, indicating that a large number of bacteria were killed, demonstrating its strong killing ability against both Gram-negative and Gram-positive bacteria. SEM results (Figure 4G) further supported the antibacterial effect from a morphological perspective. The bacterial cells in the control and DexMA groups were intact and densely arranged; in the DexMA@P@CM+NIR group, *E. coli* showed obvious cell membrane rupture and collapse, and *S. aureus* showed agglomerate dissolution and cell membrane shrinkage, suggesting that the structural integrity of the bacteria was destroyed under photothermal induction, further confirming that its bactericidal mechanism is closely related to membrane damage.[44]

3.4. Photothermal synergistic enhancement of cell activity and immune homeostasis remodeling

An ideal bone repair scaffold must not only possess excellent cell adhesion and proliferation properties but also modulate the local immune microenvironment and promote the transition from inflammation to repair.[45] Therefore, we systematically evaluated its cytocompatibility and immunomodulatory effects. Live/Dead fluorescence staining (Figure 5A) showed that after 24, 72, and 120 h of culture, all groups supported BMSC survival. However, the DexMA@P@CM + NIR group showed a significant increase in cell density and more uniform cell morphology, suggesting that the composite scaffold promoted cell proliferation via synergistic photothermal therapy.[46] Quantitative cell viability analysis (Figure 5B and 5C) further confirmed this trend: at 72 and 120 h, the viability of HUVECs and BMSCs in the DexMA@P@CM and DexMA@P@CM + NIR groups was significantly higher than that in the control group (***$p < 0.001$), demonstrating the material's excellent cytocompatibility and its ability to enhance cell proliferation through the photothermal effect. Scaffold fluorescence staining results (Figure 5D) showed that in the DexMA@P@CM + NIR group, BMSCs exhibited a more extensively spread cytoskeleton and greater apparent attachment. This characteristic has positive implications for subsequent osteogenic differentiation and matrix deposition.

Cell migration experiments further revealed the scaffold's ability to promote repair. Wound healing experiments (Figure 5E and 5G) showed that the DexMA@P@CM + NIR group had the fastest wound closure, achieving near-complete healing after 36 h. Transwell assays (Figure 5F and 5H) also demonstrated that this group exhibited the highest number of cells migrating to the lower chamber, significantly higher than the other groups (***$p < 0.001$). These results demonstrate that DexMA@P@CM significantly enhances the migration of HUVECs under photothermal treatment, providing favorable conditions for angiogenesis and bone tissue regeneration.

Regarding immune regulation, RT-qPCR results (Figure 5I) showed a significant upregulation of the anti-inflammatory cytokine IL-10 and a significant decrease in the pro-inflammatory cytokine IL-1β in the DexMA@P@CM + NIR group (***$p < 0.001$), demonstrating that the scaffold effectively inhibited inflammatory responses. iNOS/CD206 ratio analysis (Figure 5J) further demonstrated a decrease in the proportion of pro-inflammatory M1 macrophages and a significant increase in the proportion of anti-inflammatory M2 macrophages in the DexMA@P@CM+NIR group. Immunofluorescence staining results (Figure 5K) were consistent with this finding, showing increased CD206 (M2) and decreased iNOS (M1). Flow cytometry analysis (Figure 5L and 5M) provided further evidence: in the DexMA@P@CM+NIR group, the proportion of M2 macrophages was the highest (approximately 19.47%), while the proportion of M1 macrophages was the lowest, indicating that the scaffold reshapes the immune microenvironment by promoting M2 polarization and inhibiting M1 polarization.[47] These results clearly reveal that the composite scaffold can promote the transformation of macrophages into M2 macrophages through the photothermal effect and synergy with functional components, thereby reshaping the local immune microenvironment.[44]

3.5. Verification of angiogenesis and osteogenesis functions regulated by photothermal synergy.

In complex microenvironments such as diabetic bone

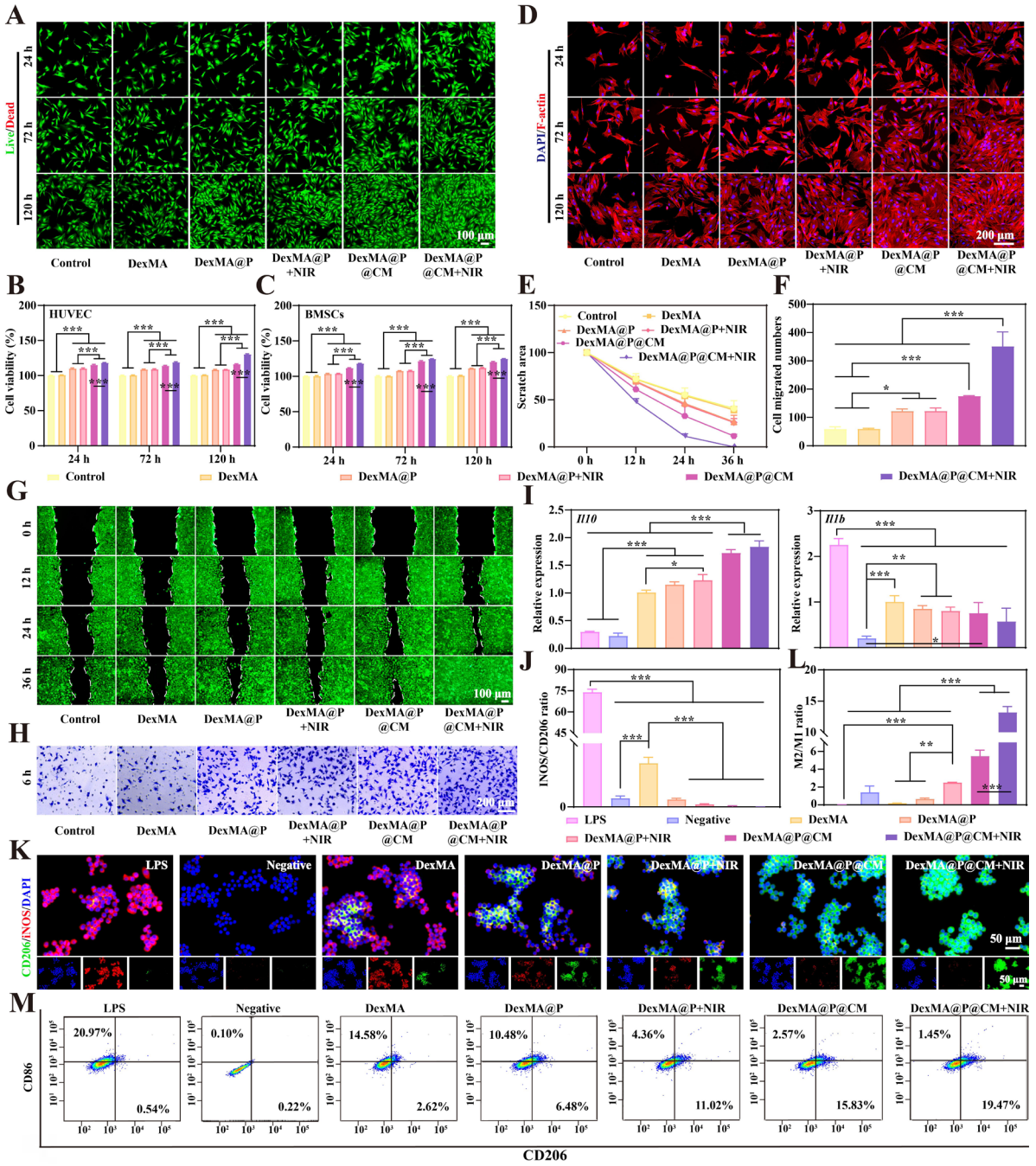


Figure 5. Evaluation of cell compatibility and immunomodulatory properties of 3D-printed composite scaffolds. (A) Fluorescent staining images of BMSCs at different time points (24, 72, 120 h). Scale bars: 100 μm; magnification: 100×. (B) Cell viability of HUVECs at different time points. (C) Cell viability of BMSCs at different time points. (D) Fluorescent staining images of the cytoskeleton of BMSCs at different time points. Scale bars: 200 μm; magnification: 200×. (E) Quantitative analysis of the residual scratch area at different time points. (F) Number of migrated cells in the Transwell assay. (G) Representative scratch-assay images. Scale bars: 100 μm; magnification: 100×. (H) Representative Transwell images after 24 h of interaction between hydrogel and HUVECs. Scale bars: 200 μm; magnification: 100×. (I) mRNA expression levels of the anti-inflammatory factor IL-10 and pro-inflammatory cytokine IL-1β. (J) Quantitative analysis of iNOS/CD206 expression. (K) Immunofluorescence staining images of iNOS and CD206. Scale bars: 50 μm; magnification: 200×. (L) Quantitative analysis of the M2/M1 ratio via flow cytometry. (M) Flow cytometry results for CD86 and CD206. $^{*}p < 0.05$, $^{**}p < 0.01$, $^{***}p < 0.001$.

Abbreviations: BMSCs: Bone marrow mesenchymal stem cells; DAPI: 4′,6-Diamidino-2-phenylindole; DexMA: Methacrylated dextran; HUVECs: Human umbilical vein endothelial cells; IL: Interleukin; iNOS: Inducible nitric oxide synthase; LPS: Lipopolysaccharide; M1: Classically activated macrophages; M2: Alternatively activated macrophages; NIR: Near-infrared.

defects, angiogenesis and bone regeneration often occur in a closely coupled process.[48] Fabricating functional scaffolds with dual regulatory capabilities is crucial for tissue regeneration.[49] To systematically validate the synergistic effects of the DexMA@P@CM composite scaffold on angiogenesis and osteogenesis, this study conducted a multidimensional assessment at the cellular, functional, and molecular mechanistic levels. As shown in Figure 6, in the tube formation experiment (Figure 6A), HUVECs formed only limited tubular networks in the DexMA and DexMA@P scaffolds. However, in the DexMA@P@CM group, the tubular structure was more complex and branched, and the network formation ability was significantly enhanced, especially after NIR light irradiation. Quantitative results further confirmed that this group showed significantly higher values than the other groups in terms of node number, total tube length, and number of branch points (Figure 6B–6D), indicating that the introduction of Cu_2O@MXene and photothermal stimulation synergistically promoted angiogenesis. To further explore the underlying mechanism, immunofluorescence analysis of angiogenesis-related factors was performed. Results showed that the expression levels of CD31, VEGF, and its receptor VEGFR2 were significantly elevated in the DexMA@P@CM + NIR group (Figure 6E–6H), suggesting that the composite scaffold may promote endothelial cell function by activating the VEGF/VEGFR2 signaling pathway. Furthermore, Western blot analysis revealed that the DexMA@P@CM + NIR group had the highest expression of CD31 and VEGF proteins (Figure 6O and 6P), further supporting its pro-angiogenic ability. This phenomenon may be attributed to the following factors: First, Cu_2O@MXene converts NIR energy into a localized heat, enhancing endothelial cell activity and migration;[50] second, the released Cu^{2+} acts as a pro-angiogenic signaling factor, inducing upregulation of VEGF expression;[51] and third, the MXene layer improves the surface charge distribution and hydration properties of the scaffold, thereby enhancing cell adhesion and proliferation.[52]

In terms of osteogenesis, ALP staining and enzyme activity assays (Figure 6I and 6J) demonstrated that the DexMA@P@CM + NIR group significantly induced early osteogenic differentiation of BMSCs under illumination, as evidenced by enhanced ALP activity. Alizarin Red S staining and quantification of mineral deposition (Figure 6K and 6L) revealed that the DexMA@P@CM scaffold induced the most calcium nodule formation under illumination, reflecting its promotion of late osteogenesis. This effect may be related to the following factors: the HAP component continuously releases calcium and phosphate ions, providing a substrate for bone matrix deposition;[53] and the NIR-induced temperature increase and dynamic changes in intracellular Ca^{2+}, which activate osteogenesis-related transcriptional pathways.[54] Further immunofluorescence staining to assess the expression of osteogenic marker proteins (Figure 6M and 6N) revealed significantly enhanced fluorescence intensity of RUNX2 and OCN in the DexMA@P@CM+NIR group, closely correlating with the level of osteogenic differentiation. Western blotting analysis further confirmed significantly elevated expression levels of key osteogenic proteins, including COL-I, β-catenin, RUNX2, ALP, and OCN (Figure 6Q and 6R), suggesting that the composite scaffold may synergistically promote bone formation by activating the Wnt/β-catenin pathway. Overall, the DexMA@P@CM composite scaffold exhibited significant effects on both angiogenesis and osteogenic differentiation, with the effects being even more pronounced under NIR illumination. This mechanism involves the coordinated regulation of multiple factors, including photothermal effects, functional ion release, and activation of cell signaling pathways.

3.6. Molecular regulatory mechanisms mediated by 3D-printed composite scaffolds.

To further elucidate the mechanisms underlying the composite scaffold's promotion of osteogenesis, angiogenesis, and immune regulation, we performed transcriptomic analysis of BMSCs after scaffold treatment to comprehensively characterize gene expression remodeling and transcriptional pathway regulation. Principal component analysis revealed a clear separation between the control and DexMA@P@CM + NIR groups along PC1 and PC2, reflecting significant differences in global gene expression patterns following the material intervention (Figure 7A). A Venn diagram (Figure 7B) revealed that the two groups shared 11,980 expressed genes, whereas 166 genes were uniquely detected in the DexMA@P@CM+NIR group, suggesting that the scaffold induces specific transcriptional regulatory programs. Furthermore, a volcano plot (Figure 7C) further identified 71 significantly upregulated and 274 significantly downregulated differentially expressed genes. The upregulated genes, such as *Cxcl1*, *Mmp9*, and *Mmp13*, are closely associated with immune chemotaxis, matrix remodeling, and osteogenesis, demonstrating the scaffold's ability to reprogram the microenvironment.[55] Inter-sample correlation analysis (Figure 7D) and a heatmap of differentially expressed genes (Figure 7E) confirmed the high reproducibility of the data and the presence of systematic genomic changes across the intervention groups. Notably, the expression of multiple osteogenesis-related transcription factors (such as *Runx2* and *Sp7*) and angiogenesis regulators (such as *Vegfa* and *Flt1*)

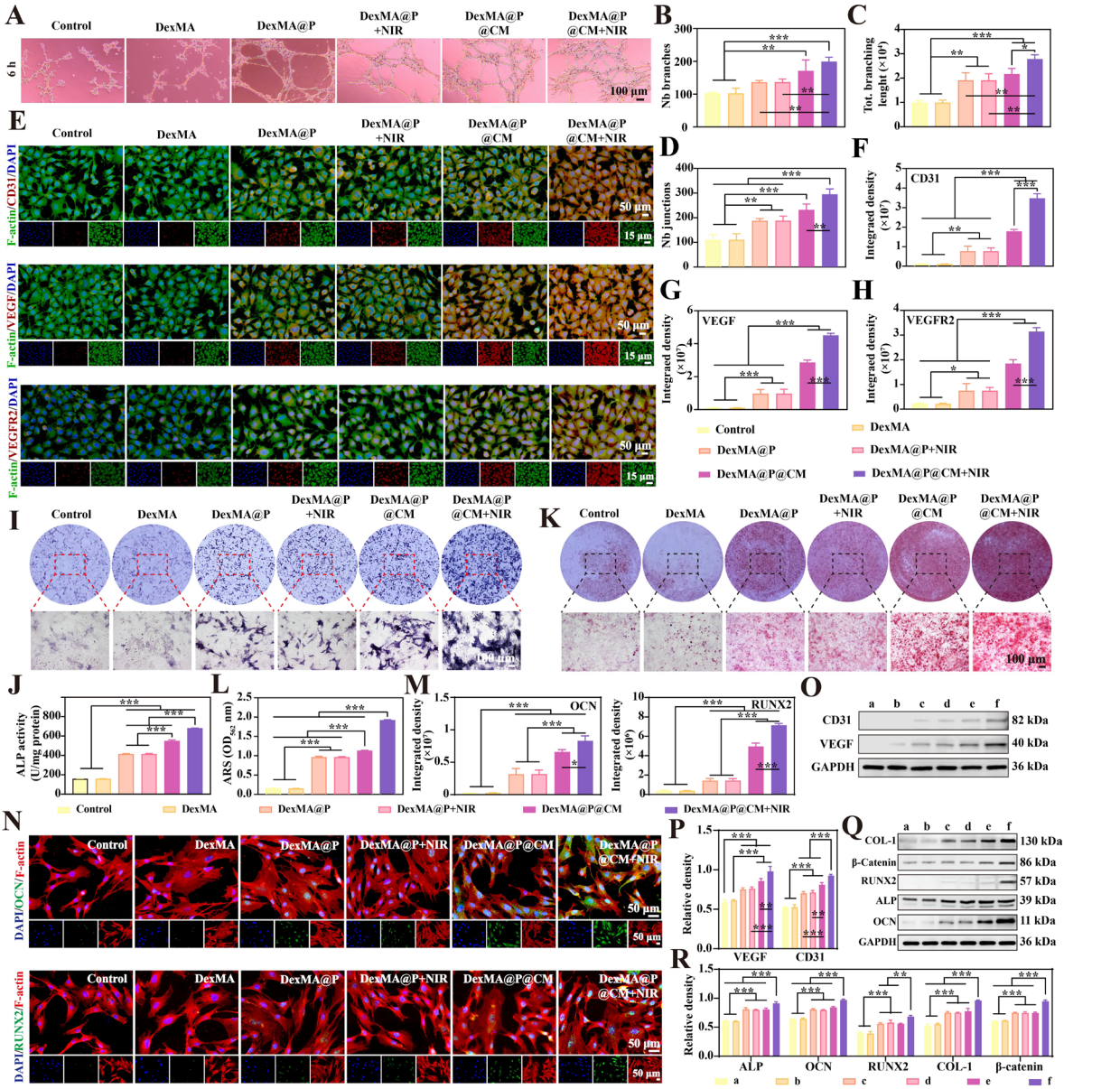


Figure 6. Evaluation of the angiogenesis and osteogenic properties of 3D-printed composite scaffolds. (A) Representative images of HUVECs after 6 h of tube formation under different scaffold conditions. The small images below show the individual fluorescence channels for DAPI, the target protein, and F-actin within the same field of view. Scale bars: 100 μm; magnification: 200×. (B–D) Quantitative analysis of (B) the number of branches, (C) total length, and (D) number of junctions. (E) Immunofluorescence staining images of CD31, VEGF, and VEGFR2 after the scaffolds were applied to HUVECs. The small images below show the individual fluorescence channels for DAPI, the target protein, and F-actin within the same field of view. Scale bars: 50 μm/15 μm; magnification: 200×. (F–H) Quantitative analysis of fluorescence intensity of angiogenesis-related proteins CD31, VEGF, and VEGFR2. (I) ALP staining images. Scale bars: 100 μm; magnification: 100×. (J) Quantitative analysis of ALP enzyme activity. (K) ARS staining images. Scale bars: 100 μm; magnification: 100×. (L) Quantitative analysis of absorbance values after ARS dye extraction corresponding to the ARS staining images. (M) Quantitative analysis of OCN and RUNX2 fluorescence intensity. (N) Representative immunofluorescence images of OCN and RUNX2. Scale bars: 50 μm; magnification: 400×. (O) Western blot analysis of the angiogenesis-related proteins CD31 and VEGF. (P) Quantitative analysis of CD31 and VEGF expression levels corresponding to the Western blot results. (Q) Western blot analysis of osteoblast markers COL-I, β-catenin, RUNX2, ALP, and OCN. (R) Quantitative analysis of relative grayscale values of COL-I, β-catenin, RUNX2, ALP, and OCN protein expression.

Note: In panels O–R, a–f represent the Control, DexMA, DexMA@P, DexMA@P+NIR, DexMA@P@CM, and DexMA@P@CM+NIR, respectively. $^{*}p < 0.05$, $^{**}p < 0.01$, $^{***}p < 0.001$.

Abbreviations: ALP: Alkaline phosphatase; ARS: Alizarin Red S; COL-I: Type I collagen; DAPI: 4′,6-Diamidino-2-phenylindole; DexMA: Methacrylated dextran; GAPDH: Glyceraldehyde-3-phosphate dehydrogenase; HUVECs: Human umbilical vein endothelial cells; NIR: Near-infrared; OCN: Osteocalcin; RUNX2: Runt-related transcription factor 2; VEGF: Vascular endothelial growth factor; VEGFR2: Vascular endothelial growth factor receptor 2.

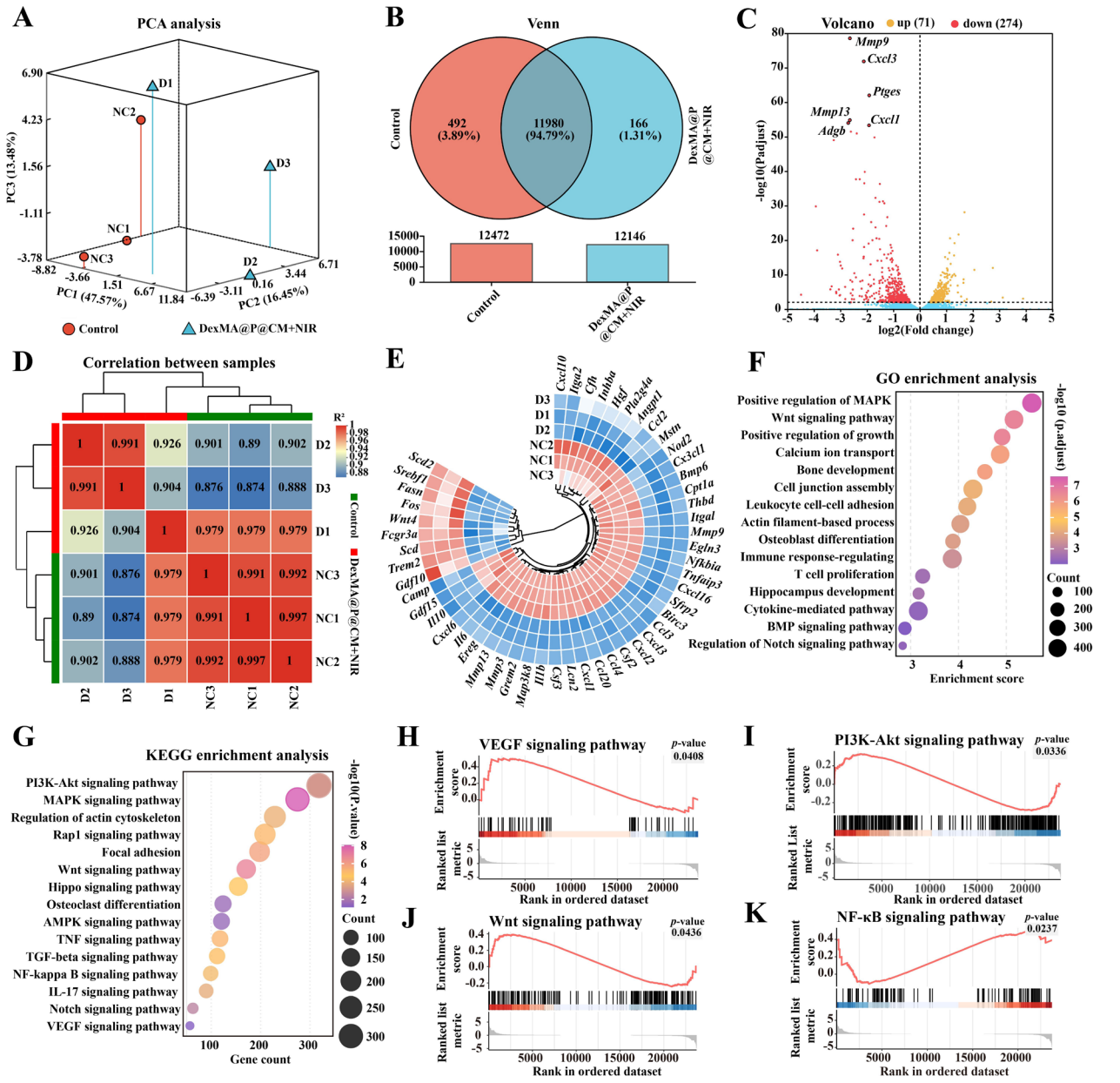


Figure 7. Transcriptome sequencing reveals the molecular regulatory mechanism of the DexMA@P@CM+NIR scaffold in bone marrow mesenchymal stem cells. (A) PCA plot. (B) Venn diagram of gene expression intersection and specificity distribution between the two groups. (C) Volcano plot of significantly differentially expressed genes between the two groups, with red indicating downregulated genes, yellow indicating upregulated genes, and gray indicating non-differential genes. (D) Expression correlation heatmap. (E) Circular clustering heatmap of differentially expressed genes. (F) GO enrichment analysis. (G) KEGG pathway enrichment. GSEA of the (H) VEGF signaling pathway, (I) PI3K–Akt signaling pathway, (J) Wnt signaling pathway, and (K) NF-κB signaling pathway.

Abbreviations: AMPK: AMP-activated protein kinase; DexMA: Methacrylated dextran; GO: Gene Ontology; GSEA: Gene set enrichment analysis; IL-17: Interleukin 17; KEGG: Kyoto Encyclopedia of Genes and Genomes; MAPK: Mitogen-activated protein kinase; NF-κB: Nuclear factor kappa B; NIR: Near-infrared; PCA: Principal component analysis; PI3K: Phosphoinositide 3-kinase; TGF-β: Transforming growth factor beta; TNF: Tumor necrosis factor; VEGF: Vascular endothelial growth factor.

was significantly upregulated in the intervention group, suggesting that the material promotes tissue regeneration by synergistically activating bone-vascular coupling pathways.[56] GO enrichment analysis (Figure 7F) further revealed that DexMA@P@CM + NIR significantly affected multiple key biological processes, including positive

regulation of mitogen-activated protein kinase (MAPK) signaling, Wnt signaling, bone tissue development, cell-cell adhesion, and regulation of the inflammatory response. This suggests that the material intervention has broad regulatory capabilities in inducing stem cell fate determination, maintaining microenvironmental immune homeostasis, and matrix remodeling. KEGG enrichment results (Figure 7G) also support this view, with differentially expressed genes concentrated in signaling pathways closely related to stem cell activity, osteogenic differentiation, and immune regulation, such as phosphoinositide 3-kinase–protein kinase B (PI3K–Akt), MAPK, Wnt, transforming growth factor beta (TGF-β), VEGF, and Nuclear factor kappa B (NF-κB). Further validation of key functional pathways using gene set enrichment analysis (GSEA) enrichment analysis (Figure 7H–7K) revealed that DexMA@P@CM + NIR significantly activated the VEGF signaling pathway (p = 0.0488), Wnt signaling pathway (p = 0.0436), and PI3K–Akt signaling pathway (p = 0.0336), while inhibiting the NF-κB signaling pathway (p = 0.0237). This further confirms that the scaffold material may exert its therapeutic advantages in angiogenesis, osteogenic and inflammatory regulation through multiple synergistic signaling pathways. Notably, the Wnt and PI3K–Akt signaling pathways play a core regulatory role in promoting MSC osteogenic differentiation, while VEGF and NF-κB respectively dominate angiogenesis and immune environment remodeling. The biological functions exhibited by these two pathways were also confirmed at the molecular level.[57-60]

3.7. Establishment of an infected calvarial defect model in diabetic rats

In previous *in vitro* experiments, we demonstrated that the DexMA@P@CM composite scaffold exhibited excellent osteoinductive, angiogenic, and immunomodulatory capabilities at the cellular level. However, infected bone defects are often characterized by persistent bacterial invasion and disturbances of the inflammatory microenvironment, which significantly hinder bone tissue regeneration.[61] Therefore, achieving both antibacterial and osteogenic repair *in vivo* is crucial. To this end, the present study systematically evaluated the bone regeneration and antibacterial properties of the DexMA@P@CM + NIR scaffold in an established infected calvarial defect model in diabetic rats (Figure 8). Micro-CT 3D reconstruction images (Figure 8A) showed that at 6 and 12 weeks post-surgery, the DexMA@P@CM + NIR group exhibited extensive, dense, and continuous new bone formation within the defect area, while the control and DexMA groups exhibited significantly less new bone mass and incomplete bone bridging. Quantitative analysis (Figure 8B) further confirmed that the BV/TV, Tb.Th, and Tb.N in the DexMA@P@CM + NIR group reached their highest levels at week 12, suggesting that the scaffold effectively promoted bone defect repair and bone microarchitecture remodeling. In the presence of infection, antibacterial ability is a prerequisite for successful bone repair.[62] Plate experiments (Figure 8C) showed that the DexMA and DexMA@P groups had limited inhibitory effect on *E. coli* and *S. aureus*, while the DexMA@P@CM+NIR group virtually eliminated the bacterial colonies, demonstrating a near-complete bactericidal effect. This result is closely related to its photothermal properties. Infrared thermal imaging (Figure 8D) showed that under 808 nm laser irradiation, the surface temperature of the DexMA@P@CM+NIR group gradually increased and reached a peak of approximately 51.2 °C after 5 min of NIR irradiation, providing a short-term thermal condition for bacterial inactivation. However, because thermal effects depend on the complete temperature–time history and tissue-specific sensitivity, the safety of this irradiation protocol for surrounding tissues requires further evaluation. This demonstrates that the efficient photothermal conversion capability of Cu_2O@MXene not only enables rapid local sterilization but also improves local blood flow and cell activity through microthermal stimulation, creating a favorable microenvironment for bone regeneration.

Hematoxylin and eosin and Masson's trichrome staining further verified bone tissue regeneration and structural remodeling (Figure 8E). Six weeks after surgery, significant new bone islands and collagen deposition were observed in the defect area of the DexMA@P@CM + NIR group, suggesting early initiation of bone repair. By week 12, the area of new bone in this group had further increased, integrating well with the host bone, and the medullary cavity structure was gradually restored. In contrast, the control and single-component groups still had large areas of unhealed bone and significant residual fibrous tissue, indicating limited repair capacity. Further analysis using Goldner's trichrome staining (Figure 8F) revealed that the DexMA@P@CM + NIR group showed a significant increase in green mineralized bone area at 6 weeks, while at 12 weeks the mineralized area almost covered the entire defect area, accompanied by significant trabecular remodeling and bone plate formation. This indicates that the system not only promotes early osteogenesis but also continuously drives the later maturation of mineralization. Combining the antibacterial and photothermal results, it can be inferred that the DexMA@P@CM + NIR composite scaffold works synergistically through the dual mechanisms of "photothermal sterilization + osteogenesis promotion" in an infected environment: on the one hand, antibacterial and infection control are achieved through photothermal

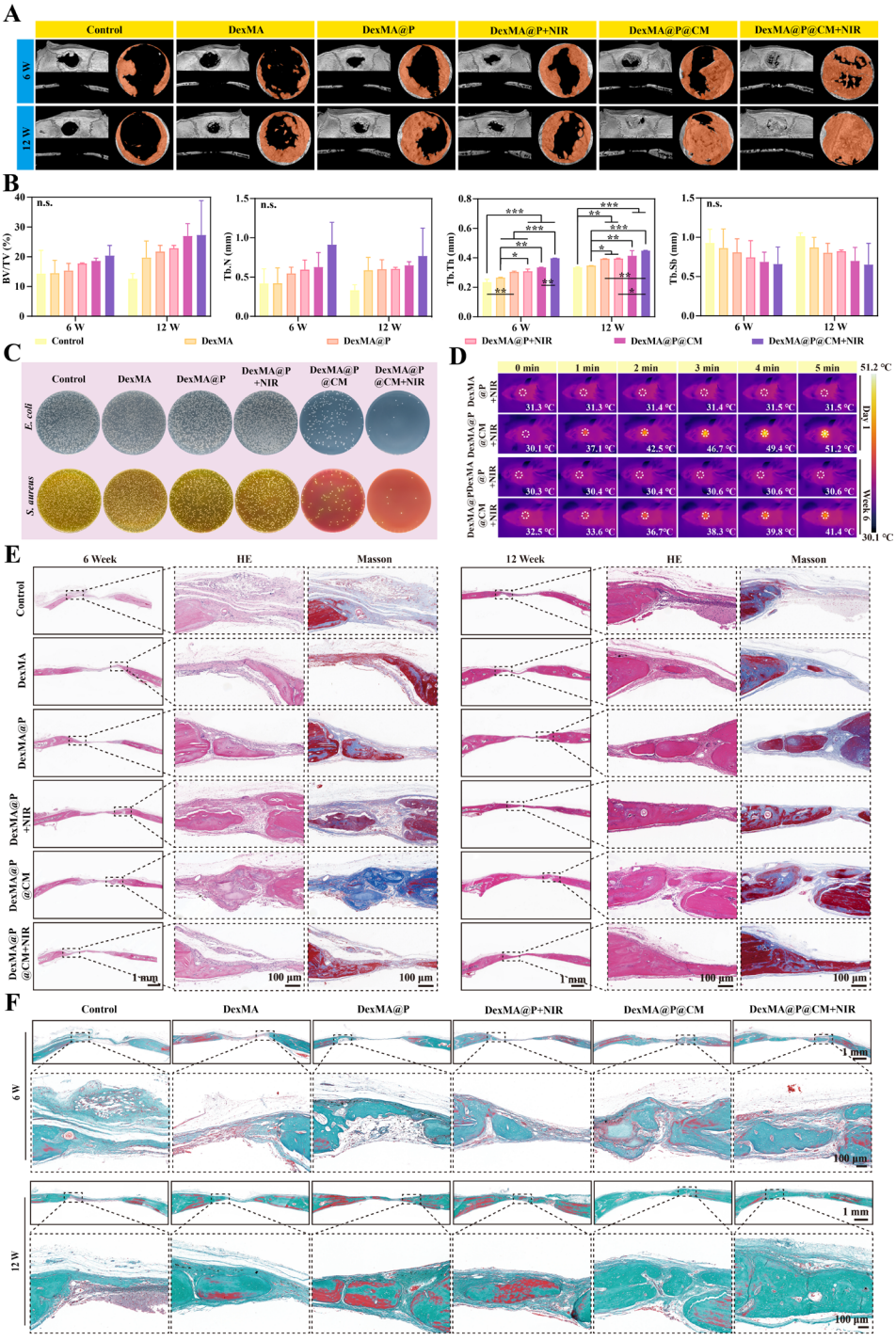


Figure 8. Composite scaffolds promote bone reconstruction in an infected bone defect model. (A) Micro-CT reconstructed image; the orange area represents newly formed bone tissue. (B) Quantitative analysis of the corresponding micro-CT images, including statistical comparisons of BV/TV, Tb.N, Tb.Th, and Tb.Sp. (C) Antibacterial activity of the scaffold against two typical bacteria (*E. coli* and *S. aureus*) in a rat infection model, expressed as colony-forming units on the plates of each group. (D) Thermal imaging of different scaffolds under near-infrared laser irradiation (808 nm, 2.0 W/cm^2). (E) Hematoxylin and eosin and Masson's trichrome staining images of the injury site after 6 and 12 weeks of composite scaffold treatment. Scale bars: 1 mm/100 μm; magnification: 10×/100×. (F) Goldner's trichrome staining of the injury site at 6 and 12 weeks after composite scaffold treatment. Scale bars: 1 mm/100 μm; magnification: 10×/100×. *$p < 0.05$, **$p < 0.01$, ***$p < 0.001$, n.s.: Non-significant.

Abbreviations: BV/TV: Bone volume fraction; DexMA: Methacrylated dextran; H&E: Hematoxylin and eosin; Micro-CT: Micro-computed tomography; NIR: Near-infrared; Tb.N: Trabecular number; Tb.Sp: Trabecular spacing; Tb.Th: Trabecular thickness.

effect and Cu^{2+} release, reducing the adverse effects of the inflammatory microenvironment;[44] on the other hand, relying on the mineralization environment provided by PDA-HAP and the signal regulation of MXene, it promotes the activation of osteogenesis-related pathways (such as Wnt/β-catenin and TGF-β), thereby accelerating bone tissue reconstruction.[63]

3.8. Longitudinal analysis of repair outcomes *in vivo*

In the microenvironment of infected bone defects, persistent bacterial colonization and the release of toxins, such as LPS, can chronically activate the innate immune response, leading to persistent overactivation of the NF-κB inflammatory pathway and resulting in the excessive secretion of inflammatory factors such as IL-1β, IL-6, and TNF-α.[64,65] These inflammatory factors not only directly inhibit the differentiation of BMSCs into the osteogenic lineage but also damage vascular endothelial cell function, forming a vicious cycle of "inflammation–osteogenic inhibition–vascular degeneration."[66] Therefore, without effective control of the infection and inflammatory microenvironment, simply providing scaffold support is insufficient to achieve effective bone regeneration. This study first evaluated the ability of different materials to regulate osteogenic differentiation using OSX immunofluorescence. As shown in Figure 9A and 9B, at 12 weeks post-surgery, the number of OSX-positive cells in the defect area of the DexMA@P@CM + NIR group was significantly increased, while the Control and non-combined groups showed only scattered weak expression. The fundamental reason for this phenomenon is that the DexMA@P@CM + NIR system effectively reduces local bacterial load through photothermal antibacterial action, thereby weakening the inhibitory effect of inflammatory signals on osteoblast differentiation at its source.[44] Previous studies have shown that signaling through the RUNX2–OSX axis is inhibited in a high IL-1β/TNF-α microenvironment.[67] This system, by reducing inflammatory factor levels, indirectly restores and enhances the activity of the RUNX2–OSX osteogenic differentiation pathway, leading to a significant upregulation of OSX expression. This also explains why, although DexMA@P@CM or DexMA@P + NIR, when used alone, can partially improve the microenvironment, their osteogenic induction ability is still significantly weaker than that of the photothermal + antibacterial dual synergistic system.

Furthermore, COL-I immunofluorescence results (Figure 9C and 9D) showed that the DexMA@P@CM + NIR group exhibited the strongest COL-I deposition at both 6 and 12 weeks. COL-I is a core structural protein in bone matrix formation, and its expression level reflects the functional output capacity of osteoblasts.[68] Its significant upregulation was not the result of a single osteogenic stimulus, but rather stemmed from a synergistic dual mechanism: on the one hand, the relief of the inflammatory microenvironment reduced the inhibitory effect of inflammatory factors on osteoblast extracellular matrix synthesis; on the other hand, the DexMA-based hydrogel provided a favorable microenvironment for cell adhesion and support, and enhanced cell–matrix interaction through CM modification, thereby further increasing the matrix secretion activity of osteoblasts.[11,69] From 6 to 12 weeks, COL-I changed from localized enhancement to a large-scale uniform distribution, indicating that this system not only promoted early bone matrix deposition but also effectively promoted the transformation of new bone from woven bone to mature lamellar bone. Angiogenesis is another key bottleneck in the repair of infected bone defects. CD31 immunofluorescence results (Figure 9E and 9F) showed that the DexMA@P@CM + NIR group had formed a large number of new blood vessels at 6 weeks, which were further enhanced at 12 weeks, showing a continuous distribution of tubular structures and significant co-localization with bone formation areas. This result indicates that the system effectively activated angiogenesis during bone repair, and that angiogenesis is a key basis for the delivery of oxygen, nutrients, and osteogenic signaling molecules, playing a decisive supporting role in the osteogenic process.[70] This reflects that the scaffold demonstrated strong *in vivo* regulation of angiogenesis–osteogenic coupling.

At the level of inflammation regulation, the immunohistochemical results of IL-1β, IL-6, and TNF-α (Figure 9G and 9H) further confirm the above inferences mechanistically. The DexMA@P@CM + NIR group showed the smallest percentage of positively stained area at both time points, and its reduction was significantly greater than that of the other groups. In particular, it could significantly inhibit the inflammatory cascade response at the 6-week time point. Combining the aforementioned photothermal antibacterial properties and the functions of the material components, it can be inferred that this scaffold achieves local photothermal sterilization under NIR excitation, effectively reducing the bacterial load in the defect area, weakening the continuous activation of the Toll-like receptor–NF-κB inflammatory signaling axis from the source, thereby reducing the expression levels of IL-1β, IL-6, and TNF-α, and alleviating the inhibitory effect of the inflammatory microenvironment on osteoblast differentiation and angiogenesis.

Compared with existing bone-repair scaffolds, the present system was specifically designed for the infected diabetic microenvironment. Metallic and polyetheretherketone implants provide reliable mechanical

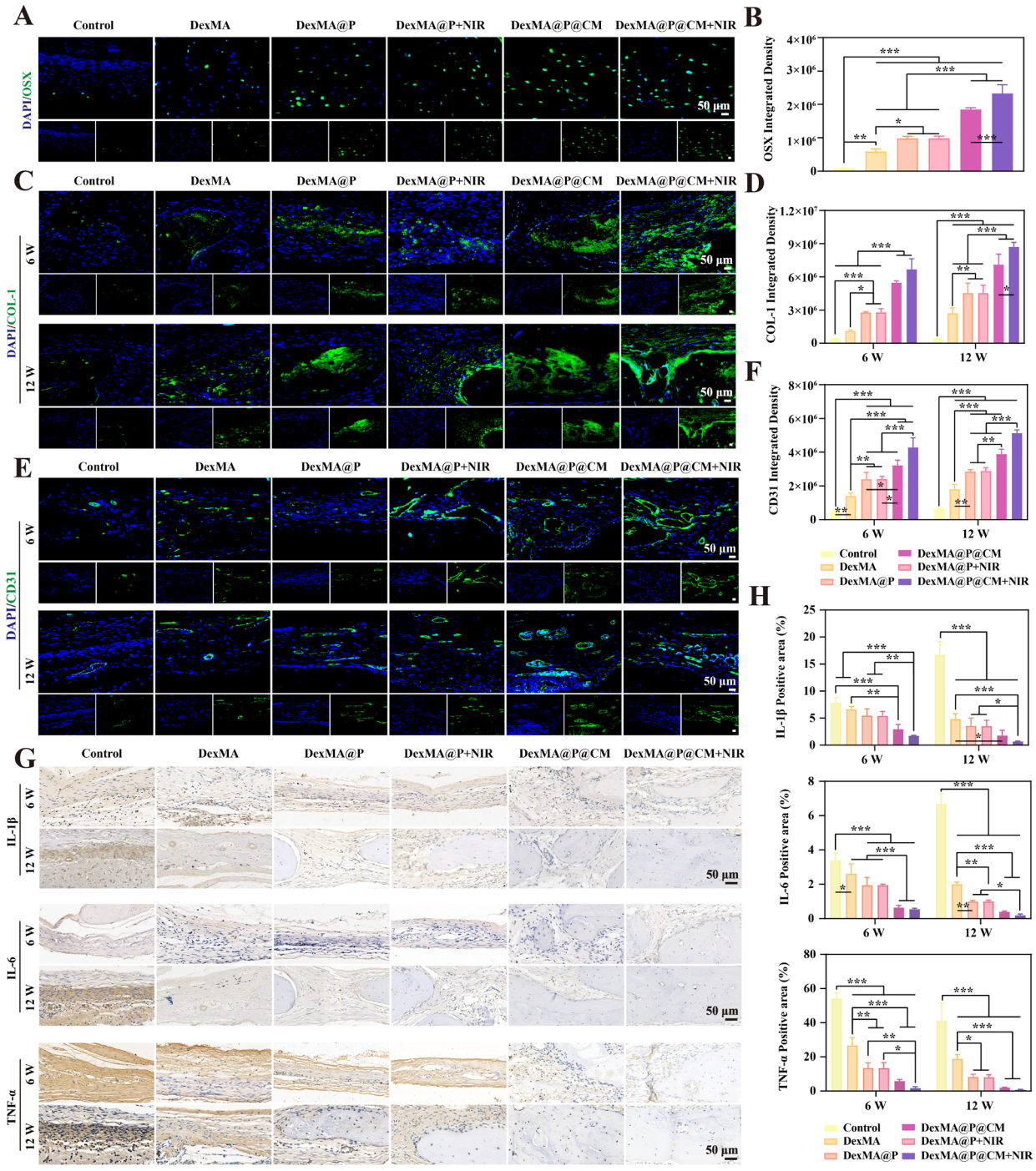


Figure 9. *In vivo* evaluation of osteogenesis, angiogenesis, and inflammatory modulation at different time points post-implantation. (A) OSX immunofluorescence staining image of the defect area at 12 weeks postoperatively. Scale bars: 50 μm; magnification: 400×. (B) Quantitative analysis of the integrated density of OSX-positive signal in each group at 12 weeks. (C) COL-I immunofluorescence staining images of the defect area at 6 and 12 weeks postoperatively. Scale bars: 50 μm; magnification: 400×. (D) Quantitative statistical results of COL-I fluorescence integrated density at different time points. (E) CD31 immunofluorescence staining images of the defect area at 6 and 12 weeks postoperatively. Scale bars: 50 μm; magnification: 400×. (F) Quantitative analysis of the integrated density of CD31-positive signal in each group. (G) Immunohistochemical staining images of inflammatory factors (IL-1β, IL-6, and TNF-α) in the defect area at 6 and 12 weeks postoperatively. Scale bars: 50 μm; magnification: 200×. (H) Quantitative analysis of the proportions of IL-1β-, IL-6-, and TNF-α-positive areas in different groups at 6 and 12 weeks. *$p < 0.05$, **$p < 0.01$, ***$p < 0.001$.

Abbreviations: COL-I: Type I collagen; DAPI: 4′,6-Diamidino-2-phenylindole; DexMA: Methacrylated dextran; IL: Interleukin; NIR: Near-infrared; OSX: Osterix; TNF-α: Tumor necrosis factor alpha.

support but generally lack intrinsic antibacterial and regenerative activity, whereas bioceramic scaffolds are primarily osteoconductive and have limited capacity to regulate infection and inflammation.[71,72] Cell- or growth-factor-loaded scaffolds may enhance regeneration but face challenges in biological stability and clinical translation.[73] In contrast, the DexMA/P-HAP/Cu_2O@MXene scaffold integrates customizable 3D printing with staged photothermal antibacterial treatment, osteogenic induction, immunomodulation, and angiogenic stimulation. In particular, sequential temperature control at 50 °C and 41 °C enables early infection control followed by mild photothermal stimulation of tissue regeneration, distinguishing this system from conventional single-temperature photothermal scaffolds.

Importantly, the scaffold was designed as a cell-free platform intended to support in situ regeneration through its porous structure and the delivery of osteogenic, immunomodulatory, and angiogenic signals. However, its efficacy was evaluated solely in a rat calvarial defect model featuring a simple geometry and a 5 mm diameter, a setup that failed to adequately replicate the clinical conditions of diabetic bone defects, including size, thickness, mechanical environment, or chronic pathological characteristics. Furthermore, the study did not directly track the origins of infiltrating host cells or their distribution patterns relative to depth. Additionally, the specific contribution of the 3D-printed structure to tissue regeneration remains unclear, as no identical composition cast scaffolds were included as controls. Therefore, future research will compare printed scaffolds with cast scaffolds, track host cell infiltration, evaluate the long-term biosafety of Cu_2O@MXene and NIR-induced heat generation, and validate regenerative efficacy in large-animal models of critical-sized bone defects.

4. Conclusion

This study designed and constructed a DexMA/P-HAP/Cu_2O@MXene composite scaffold that combines structural printability, bioactivity, and intelligent responsiveness to address the multiple challenges of repairing diabetes-associated infected bone defects. The scaffold utilizes DexMA to construct a 3D framework that exhibits excellent mechanical stability and formability. PDA-HAP enhances the inorganic-matrix bonding and osteogenic induction. The Cu_2O@MXene nanoplatform achieves a NIR-triggered dual-temperature photothermal response, enabling sequential switching between sterilization (50 °C) and osteogenic regulation (41 °C). The synergistic release of Cu^{2+} ions contributes to its multiple functions, including antibacterial, angiogenic, and immunomodulatory activities. Mechanism studies have shown that the scaffold can significantly scavenge ROS *in vitro*, inhibit the expression of inflammatory factors, induce macrophage polarization toward an M2 phenotype, and activate VEGF signaling *in vivo*, thereby promoting angiogenesis. At the same time, it upregulates the expression of bone markers such as OSX and COL-I, accelerates new bone formation and defect repair, and supports a proposed "photothermal–immune–vascular–osteogenesis" multi-pathway synergistic reconstruction mechanism. In the complex environment of diabetes, the scaffold exhibits excellent antibacterial, osteogenic, and tissue-integration capabilities. Collectively, this modular scaffold provides a promising acellular strategy for treating diabetic infected bone defects. It can be further developed into a controlled therapeutic-delivery platform that can be dynamically monitored and regulated by integrating drug sustained-release systems or biosensor elements, providing new strategic support for bone regeneration treatment related to diabetes and other chronic diseases.

Acknowledgments

None.

Funding

This study was supported by the National Natural Science Foundation of China (82571054).

Conflict of interest

The authors declare no competing financial interests.

Author contributions

Conceptualization: Ye Wang
Data curation: Ye Wang
Formal analysis: Zonghe Xu
Funding acquisition: Lin Zhou
Investigation: Dong Wu
Visualization: Dong Wu
Project administration: Lin Zhou
Writing–original draft: Jiao Hu
Writing–review & editing: Qingxia Fang, Bixia Li

Ethics approval and consent to participate

This study adhered to the Principles of Laboratory Animal Care (National Institutes of Health Publication No. 85-23, revised 1996) and was approved by the National Institutional Animal Care Committee. The animal ethics approval number is 202501007.

Consent for publication

Not applicable.

Availability of data

The data supporting the findings of this study are available within the article and its supplementary materials. Additional raw data are available from the corresponding author upon reasonable request.

References

1. Lou X, Wang F, Lv X, *et al*. Sequential angiogenic-osteogenic coupling via a spatiotemporally graded hydrogel enables vascularized bone organoids for critical-sized calvarial defect reconstruction. *Compos B Eng.* 2025;302:112553.

   doi: 10.1016/j.compositesb.2025.112553

2. Xi Y, Zhang Z, Zhao Z, *et al*. Injectable thymosin β4-modified hyaluronic acid hydrogel with exosomes for stem cell homing and neuronic–angiogenic–osteogenic coupled cranial repair. *ACS Nano.* 2025;19(25):22710-22724.

   doi: 10.1021/acsnano.4c10386

3. Si Y, Li X, Dong S, *et al*. Hydrogel scaffold encapsulating MSC-Exos and ZIF-8 promotes bone regeneration via coordinating osteogenesis and immunomodulation. *Bioact Mater.* 2025;54:329-351.

   doi: 10.1016/j.bioactmat.2025.08.026

4. Wang D, Wang Y, Song D, *et al*. Microgels-encapsulated magnesium/emodin-based metal organic framework nanorods for diabetic bone regeneration. *Chem Eng J.* 2024;487:150585.

   doi: 10.1016/j.cej.2024.150585

5. Sheng N, Xing F, Zhang QY, *et al*. A pleiotropic SIS-based hydrogel with immunomodulation via NLRP3 inflammasome inhibition for diabetic bone regeneration. *Chem Eng J.* 2024;480:147985.

   doi: 10.1016/j.cej.2023.147985

6. Mu W, Liang G, Feng Y, Jiang Y, Qu F. The potential therapeutic role of metformin in diabetic and non-diabetic bone impairment. *Pharmaceuticals (Basel).* 2022;15(10):1274.

   doi: 10.3390/ph15101274

7. Li J, Fan M, Jiao Z, *et al*. Glucose-gated nanocoating endowing polyetheretherketone implants for enzymatic gas therapy to boost infectious diabetic osseointegration. *Nano Today.* 2024;59:102541.

   doi: 10.1016/j.nantod.2024.102541

8. Xu X, Zuo J, Zeng H, *et al*. Improving osseointegration potential of 3D printed PEEK implants with biomimetic periodontal ligament fiber hydrogel surface modifications. *Adv Funct Mater.* 2024;34(14):2308811.

   doi: 10.1002/adfm.202308811

9. Li W, Kang J, Yuan Y, *et al*. Preparation and characterization of PVA-PEEK/PVA-β-TCP bilayered hydrogels for articular cartilage tissue repair. *Compos Sci Technol.* 2016;128:58-64.

   doi: 10.1016/j.compscitech.2016.03.013

10. Wang L, Wei L, Wei J, *et al*. 3D printed porous PEEK scaffolds with stable and durable gelatin composite hydrogel coating loaded Yoda1 for in vivo osseointegration. *Int J Biol Macromol.* 2025;307:141577.

    doi: 10.1016/j.ijbiomac.2025.141577

11. Huang Y, Chen T, Ren C, *et al*. High-strength gelatin hydrogel scaffold with drug loading remodels the inflammatory microenvironment to enhance osteoporotic bone repair. *Adv Mater.* 2025;37(13):e2501051.

    doi: 10.1002/adma.202501051

12. Zhou L, Liu H, Zhang B, *et al*. A novel 3D-printed bi-layer cranial-brain patch promotes brain injury repair and bone tissue regeneration. *Adv Funct Mater.* 2024;34(18):2314330.

    doi: 10.1002/adfm.202314330

13. Ng WL, Bartolo P. 3D bioprinting of tissues and organs for systemic diseases and localized injuries. *Mil Med Res.* 2026;13(1):100006.

    doi: 10.1016/j.mmr.2026.100006

14. Zhang Y, Sun Y, Luo J, *et al*. Hydrogel-based materials for mandibular reconstruction. *Mater Sci Add Manuf.* 2025;4(2):025070006.

    doi: 10.36922/MSAM025070006

15. Yu K, Yao Y, Gao Q, *et al*. Investigation of humidity-driven swelling–shrinking behavior of filaments in material extrusion of medical-grade biodegradable hydrogel. *Int J Bioprint.* 2025;11(4):409-425.

    doi: 10.36922/IJB025220222

16. Blache U, Ford EM, Ha B, *et al*. Engineered hydrogels for mechanobiology. *Nat Rev Methods Primers.* 2022;2(1):98.

    doi: 10.1038/s43586-022-00179-7

17. Xie D, Hu C, Zhu Y, *et al*. Sequential therapy for osteosarcoma and bone regeneration via chemodynamic effect and cuproptosis using a 3D-printed scaffold with TME-responsive hydrogel. *Small.* 2025;21(5):e2406639.

    doi: 10.1002/smll.202406639

18. Chen G, Chen C, Dong Z, *et al*. Enhancing degradation behaviour, osteogenic capacity and angiogenic performance of additively manufactured porous Zn-Mg scaffold via a neobavaisoflavone-doped GelMA composite hydrogel coating. *Virtual Phys Prototyp.* 2025;20(1):e2500673.

    doi: 10.1080/17452759.2025.2500673

19. Liu A, Zhang Z, Wang X, *et al*. The critical role of surface characteristics in 3D-printed biodegradable Zn-based porous scaffolds for bone defect repair. *Virtual Phys Prototyp.* 2025;20(1):e2476035.

    doi: 10.1080/17452759.2025.2476035

20. Overchuk M, Weersink RA, Wilson BC, Zheng G. Photodynamic and photothermal therapies: synergy opportunities for nanomedicine. *ACS Nano.* 2023;17(9):7979-8003.

doi: 10.1021/acsnano.3c00891

21. Qi J, Si C, Liu H, *et al*. Advances of metal-based nanomaterials in the prevention and treatment of oral infections. *Adv Healthc Mater.* 2025;14(15):e2500416.

doi: 10.1002/adhm.202500416

22. Wang Z, Huang Y, He S, *et al*. Oxygen-independent sulfate radical and Fe^{2+}-modified implants for fast sterilization and osseointegration of infectious bone defects. *ACS Nano.* 2025;19(19):18804-18823.

doi: 10.1021/acsnano.5c04147

23. Chen Y, Cheng W, Tian H, Wang Y, He W, Huang C. ROS-responsive nanoassembly co-delivering chlorogenic acid and copper accelerates healing of infected burns via oxidative stress mitigation and macrophage M2 polarization. *Chem Eng J.* 2025;522:168204.

doi: 10.1016/j.cej.2025.168204

24. Yu Y, Zhao X, Zheng Y, Xia D, Liu Y. Core-shell structured CeO_2@ZIF-8 nanohybrids regulating the Ce(III)/Ce(IV) valence conversion to enhance ROS-scavenging capacity for periodontitis treatment. *Biomaterials.* 2026;325:123588.

doi: 10.1016/j.biomaterials.2025.123588

25. Wan S, Chen Y, Huang C, *et al*. Scalable ultrastrong MXene films with superior osteogenesis. *Nature.* 2024;634(8036):1103-1110.

doi: 10.1038/s41586-024-08067-8

26. Dai Y, Ma Z, Shi Z, *et al*. Microneedle arrays for near-infrared-controlled insulin delivery based on thermosensitive microgel. *ACS Appl Mater Interfaces.* 2025;17(23):33483-33497.

doi: 10.1021/acsami.5c03807

27. Darmau B, Sacchi M, Texier I, Gross AJ. Self-extracting dextran-based hydrogel microneedle arrays with an interpenetrating bioelectroenzymatic sensor for transdermal monitoring with matrix protection. *Adv Healthc Mater.* 2025;14(2):e2403209.

doi: 10.1002/adhm.202403209

28. Huang B, Chen M, Tian J, *et al*. Oxygen-carrying and antibacterial fluorinated nano-hydroxyapatite incorporated hydrogels for enhanced bone regeneration. *Adv Healthc Mater.* 2022;11(12):e2102540.

doi: 10.1002/adhm.202102540

29. Wang F, Tian F, Xia X, *et al*. One-step synthesis of organic terminal 2D $Ti_3C_2T_x$ MXene nanosheets by etching of Ti_3AlC_2 in an organic Lewis acid solvent. *Angew Chem Int Ed Engl.* 2024;63(23):e202405315.

doi: 10.1002/anie.202405315

30. Liu B, Chen X, Zhu Y, *et al*. One-step symbiosis of bimetallic peroxides nanoparticles to induce ferroptosis/cuproptosis and activate cGAS-STING pathway for enhanced tumor immunotherapy. *Adv Mater.* 2025;37(21):e2500337.

doi: 10.1002/adma.202500337

31. Fu T, Sullivan DP, Gonzalez AM, *et al*. Mechanotransduction via endothelial adhesion molecule CD31 initiates transmigration and reveals a role for VEGFR2 in diapedesis. *Immunity.* 2023;56(10):2311-2324.e6.

doi: 10.1016/j.immuni.2023.08.001

32. Jing X, Xu C, Su W, *et al*. Photosensitive and conductive hydrogel induced innerved bone regeneration for infected bone defect repair. *Adv Healthc Mater.* 2023;12(3):e2201349.

doi: 10.1002/adhm.202201349

33. Zhao Y, Kang H, Xia Y, Sun L, Li F, Dai H. 3D printed photothermal scaffold sandwiching bacteria inside and outside improves the infected microenvironment and repairs bone defects. *Adv Healthc Mater.* 2024;13(6):e2302879.

doi: 10.1002/adhm.202302879

34. Jin Y, Shu M, Liu Z, *et al*. Bio-functional immunomodulatory europium-doped hydroxyapatite nanorods for osteochondral repair via CDH5-RAS-RAF-MEK-ERK-CSF1 axis. *Chem Eng J.* 2024;484:149311.

doi: 10.1016/j.cej.2024.149311

35. Hao M, Zhang Z, Liu C, *et al*. Hydroxyapatite nanorods function as safe and effective growth factors regulating neural differentiation and neuron development. *Adv Mater.* 2021;33(33):e2100895.

doi: 10.1002/adma.202100895

36. Wei HH, Zhang XX, Sun SW, Gai SL, Yu HT, Xie Y. Interface engineering to optimize the catalytic activity of Fe, Co, and Ti sites in FeCoP/MXene toward efficient overall water splitting. *Rare Met.* 2025;44(10):7385-7403.

doi: 10.1007/s12598-025-03461-1

37. Davidson CD, Wang WY, Zaimi I, Jayco DKP, Baker BM. Cell force-mediated matrix reorganization underlies multicellular network assembly. *Sci Rep.* 2019;9(1):12.

doi: 10.1038/s41598-018-37044-1

38. Li B, Fu Q, Lu Y, *et al*. 3D hydrogel platform with macromolecular actuators for precisely controlled mechanical forces on cancer cell migration. *Nat Commun.* 2025;16(1):4831.

doi: 10.1038/s41467-025-60062-3

39. Mujtaba AG, Karakeçili A, Topuz B, *et al*. Tri-layered bioactive cutaneous scaffold with integrated bioactive metal organic frameworks to promote full-thickness infected diabetic wound healing: multifaceted therapeutic strategies. *Adv Healthc Mater.* 2025;14(15):e2500356.

doi: 10.1002/adhm.202500356

40. Li Y, Wang Y, Ding Y, *et al*. A double network composite hydrogel with self-regulating Cu^{2+}/luteolin release and mechanical modulation for enhanced wound healing. *ACS Nano.* 2024;18(26):17251-17266.

doi: 10.1021/acsnano.4c04816

41. Xiong P, Wei X, Zhou L, *et al*. Near-infrared light-triggered MXene nanocomposite for tumor-specific mild photothermal-enhanced chemodynamic therapy. *Adv Funct Mater.* 2024;34(44):2405124.

doi: 10.1002/adfm.202405124

42. Wei Q, An Y, Zhao X, Li M, Zhang J, Cui N. Optimal design of multi-biomaterials mixed extrusion nozzle for 3D bioprinting considering cell activity. *Virtual Phys Prototyp.* 2025;20(1):e2438897.

doi: 10.1080/17452759.2024.2438897

43. Yücer S, Sarac B, Karaduman E, Erarslan A, Ciftci F. 3D bioprinting scaffold of gelatine reinforced-zinc nanoparticles synthesized by green synthesis: comparative evaluation of mechanical and thermal properties. *J Mol Struct.* 2026;1357:145214.

doi: 10.1016/j.molstruc.2025.145214

44. Li X, Yang Y, Chen M, *et al*. Diatom-inspired scaffold for infected bone defect therapy: achieving stable photothermal properties and coordinated antibacterial-osteogenic functions. *Adv Mater.* 2026;38(1):e09997.

doi: 10.1002/adma.202509997

45. Chen X, Li W, Ma Y, *et al*. Nano-assisted dynamically assembled hydrogels with strong tissue adhesion and proactive immunomodulation for bone defect repair. *Bioact Mater.* 2025;53:480-494.

doi: 10.1016/j.bioactmat.2025.07.038

46. Yang C, Ma H, Wang Z, *et al*. 3D printed wesselsite nanosheets functionalized scaffold facilitates NIR-II photothermal therapy and vascularized bone regeneration. *Adv Sci (Weinh).* 2021;8(20):e2100894.

doi: 10.1002/advs.202100894

47. Wang Q, Li Z, Zhang Y, *et al*. Multiphase mineralized collagen scaffold for infected bone regeneration through oxidative metabolism modulation. *Adv Funct Mater.* 2025;35(32):2500593.

doi: 10.1002/adfm.202500593

48. Feng Q, Che L, Li C, *et al*. Bioadaptable 3D printed scaffold for microenvironment-activatable visualization and osteogenesis in diabetic bone defect. *Adv Funct Mater.* 2025;35(29):2500320.

doi: 10.1002/adfm.202500320

49. Wu D, Eugenis I, Hu C, *et al*. Bioinstructive scaffolds enhance stem cell engraftment for functional tissue regeneration. *Nat Mater.* 2025;24(9):1364-1374.

doi: 10.1038/s41563-025-02212-y

50. Chen J, Chen Q, Qin X, *et al*. Bacteria-targeted single-atom nanozyme with photothermal-augmented multi-enzymatic cascade and NO delivery for enhanced infected wound healing. *Adv Sci (Weinh).* 2025;12(42):e09621.

doi: 10.1002/advs.202509621

51. Qiu L, Ma S, Yang R, *et al*. Ultrasound-activated piezoelectric heterojunction drives nanozyme catalysis to induce bacterial cuproptosis-like death and promote bone vascularization and osseointegration. *Biomaterials.* 2025;320:123249.

doi: 10.1016/j.biomaterials.2025.123249

52. Wang W, Ma Z, He L, *et al*. Roles of MXene-integrated multifunctional hydrogels in tissue regeneration therapy: construction, mechanisms, and biomedical applications. *Mater Today.* 2025;89:402-439.

doi: 10.1016/j.mattod.2025.07.031

53. Bai Y, Wang Z, He X, *et al*. Application of bioactive materials for osteogenic function in bone tissue engineering. *Small Methods.* 2024;8(8):e2301283.

doi: 10.1002/smtd.202301283

54. Wang H, Zhang J, Li Z, *et al*. NIR-programmable 3D-printed shape-memory scaffold with dual-thermal responsiveness for precision bone regeneration and bone tumor management. *J Nanobiotechnology.* 2025;23(1):300.

doi: 10.1186/s12951-025-03375-1

55. Yan M, Xiao B, Yosick A, Liu B, Awad HA. Dose-dependent osteoimmunomodulatory effects of amorphous calcium phosphate nanoparticles promote 3D-printed scaffold-mediated bone regeneration. *Bioact Mater.* 2025;51:197-210.

doi: 10.1016/j.bioactmat.2025.05.010

56. Yamashita Y, Hayashi M, Liu A, *et al*. Fam102a translocates Runx2 and Rbpjl to facilitate Osterix expression and bone formation. *Nat Commun.* 2025;16(1):9.

doi: 10.1038/s41467-024-55451-z

57. Sheng C, Zhou X, Wang J, *et al*. Jiawei Yanghe decoction alleviates osteoporotic osteoarthritis by promoting MSC osteogenic differentiation and homing via ITGB6/TGF-β/CXCR4 pathway. *Phytomedicine.* 2025;147:157203.

doi: 10.1016/j.phymed.2025.157203

58. Zhang Q, Hu S, Wu J, *et al*. Nystose attenuates bone loss and promotes BMSCs differentiation to osteoblasts through BMP and Wnt/β-catenin pathway in ovariectomized mice. *Food Sci Hum Wellness.* 2023;12(2):634-646.

doi: 10.1016/j.fshw.2022.07.066

59. Mao H, Zhao X, Sun SC. NF-κB in inflammation and cancer. *Cell Mol Immunol.* 2025;22(8):811-839.

doi: 10.1038/s41423-025-01310-w

60. Lee C, Kim MJ, Kumar A, Lee HW, Yang Y, Kim Y. Vascular endothelial growth factor signaling in health and disease: from molecular mechanisms to therapeutic perspectives. *Signal Transduct Target Ther.* 2025;10(1):170.

doi: 10.1038/s41392-025-02249-0

61. Zhang R, Stehle Y, Chen L, *et al*. Multifunctional, enzyme/pH-responsive gelatin microspheres with aptamer-targeted antibacterial and ionic-mediated dual therapy for infected bone defects. *Biomaterials.* 2026;326:123642.

doi: 10.1016/j.biomaterials.2025.123642

62. Duan Y, Li Y, Wang Y, *et al*. An all-in-one "multifunctional hydrogel": through antibacterial, anti-inflammatory, and angiogenic to promoting MRSA-infected bone defect repair. *Chem Eng J.* 2025;503:158132.

doi: 10.1016/j.cej.2024.158132

63. Zhang Y, Wang T, Chen Y, *et al*. Biodegradable piezoelectric nanofibers with MXene-enhanced self-polarization for ultrasound-accelerated bone regeneration. *Nano Energy.* 2025;145:111432.

doi: 10.1016/j.nanoen.2025.111432

64. Yang Q, Lou S, Zhang Y, *et al*. NIR-II responsive multifunctional scaffold enabling "Kill-Modulation-Build" synergistic therapy for infectious bone defects. *Adv Sci (Weinh).* 2025;12(47):e08948.

doi: 10.1002/advs.202508948

65. Chen Q, Ma J, Yu S, *et al*. "Small dots, multiple functions": unveiling the veil of a bioactive quercetin carbon dot and its multifaceted antibacterial and osteogenesis mechanisms for infectious bone defect repair. *Adv Funct Mater.* 2025;35(46):2507840.

doi: 10.1002/adfm.202507840

66. Liu S, Wang Z, Li Y, *et al*. Erythropoietin-stimulated macrophage-derived extracellular vesicles in chitosan hydrogel rescue BMSCs fate by targeting EGFR to alleviate inflammatory bone loss in periodontitis. *Adv Sci (Weinh).* 2025;12(23):e2500554.

doi: 10.1002/advs.202500554

67. Zeng D, Umar M, Zhu Z, *et al*. Development of novel osteoarthritis therapy by targeting AMPK-β-catenin-RUNX2 signaling. *Genes Dis.* 2025;12(1):101247.

doi: 10.1016/j.gendis.2024.101247

68. Yang XD, Haga CL, Phinney DG. Signaling dynamics in osteogenesis: unraveling therapeutic targets for bone generation. *Curr Drug Targets.* 2025;26(5):350-366.

doi: 10.2174/0113894501359782241216082049

69. Pang Y, Wang X, Zhang H, *et al*. RGD-grafted dextran methacrylate hydrogel incorporating osteogenic peptide and Mn_3O_4 nanozymes for enhanced bone defect healing. *Mater Today Bio.* 2025;35:102436.

doi: 10.1016/j.mtbio.2025.102436

70. Li S, Cai X, Guo J, *et al*. Cell communication and relevant signaling pathways in osteogenesis–angiogenesis coupling. *Bone Res.* 2025;13(1):45.

doi: 10.1038/s41413-025-00417-0

71. Wang Z, Tang Y, Wang P, *et al*. Dynamical integration of antimicrobial, anti-inflammatory, and pro-osteogenic activities on polyetheretherketone via a porous N-halamine polymeric coating. *Adv Funct Mater.* 2023;33(41):2307286.

doi: 10.1002/adfm.202307286

72. Nguyen NH, Zhang P, Kadavan FSP, *et al*. Multifunctional hydroxyapatite coated with gallium liquid metal-based silver nanoparticles for infection prevention and bone regeneration. *Adv Funct Mater.* 2025;35(37):2423496.

doi: 10.1002/adfm.202423496

73. Shan BH, Wu FG. Hydrogel-based growth factor delivery platforms: strategies and recent advances. *Adv Mater.* 2024;36(5):e2210707.

doi: 10.1002/adma.202210707

Appendix

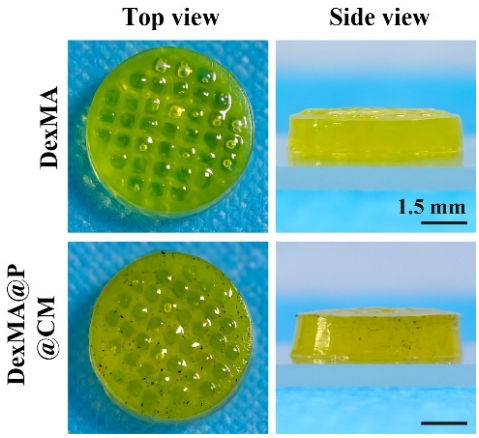


Figure A1. Representative macroscopic morphology of the fabricated scaffolds. Top and side views of the DexMA and DexMA@P@CM scaffolds fabricated by digital light processing-based vat photopolymerization. The cylindrical scaffolds were designed with dimensions of 5.0 mm in diameter and 1.5 mm in thickness. Scale bars: 1.5 mm.